nature cell biology

Technical Report

https://doi.org/10.1038/s41556-022-01005-8

A general approach to identify cell-permeable and synthetic anti-CRISPR small molecules

Received: 16 September 2021

Accepted: 2 September 2022

Published online: 17 November 2022

Check for updates

Donghyun Lim[1,2,9,10], Qingxuan Zhou[1,2,10], Kurt J. Cox[1,2,10], Benjamin K. Law[1,2,10], Miseon Lee[1,2,10], Praveen Kokkonda[1,2,10], Vedagopuram Sreekanth[1,2,3,10], Rajaiah Pergu[1,2], Santosh K. Chaudhary[1,2], Soumyashree A. Gangopadhyay[1,2,3], Basudeb Maji[1,2,3], Sophia Lai[1,4], Yuka Amako[4], David B. Thompson[5,6], Hari K. K. Subramanian[7], Michael F. Mesleh[8], Vlado Dančík[1], Paul A. Clemons[1], Bridget K. Wagner[1], Christina M. Woo[4], George M. Church[5,6] & Amit Choudhary[1,2,3] ✉

The need to control the activity and fidelity of CRISPR-associated nucleases has resulted in a demand for inhibitory anti-CRISPR molecules. The small-molecule inhibitor discovery platforms available at present are not generalizable to multiple nuclease classes, only target the initial step in the catalytic activity and require high concentrations of nuclease, resulting in inhibitors with suboptimal attributes, including poor potency. Here we report a high-throughput discovery pipeline consisting of a fluorescence resonance energy transfer-based assay that is generalizable to contemporary and emerging nucleases, operates at low nuclease concentrations and targets all catalytic steps. We applied this pipeline to identify BRD7586, a cell-permeable small-molecule inhibitor of SpCas9 that is twofold more potent than other inhibitors identified to date. Furthermore, unlike the reported inhibitors, BRD7586 enhanced SpCas9 specificity and its activity was independent of the genomic loci, DNA-repair pathway or mode of nuclease delivery. Overall, these studies describe a general pipeline to identify inhibitors of contemporary and emerging CRISPR-associated nucleases.

Clustered regularly interspaced short palindromic repeats (CRISPR)-associated nucleases (for example, *Streptococcus pyogenes* Cas9 (SpCas9), *Staphylococcus aureus* Cas9 (SaCas9) and Cas12) are programmable RNA-guided endonucleases used to induce site-specific DNA-strand breaks but their non-specific or excessive activity can have deleterious consequences[1–5]. As the specificity of such strand breaks can depend on extrinsic factors, such as nuclease concentration and activity duration, the need to control these factors has propelled the discovery

[1]Chemical Biology and Therapeutics Science, Broad Institute of MIT and Harvard, Cambridge, MA, USA. [2]Department of Medicine, Harvard Medical School, Boston, MA, USA. [3]Divisions of Renal Medicine and Engineering, Brigham and Women's Hospital, Boston, MA, USA. [4]Department of Chemistry and Chemical Biology, Harvard University, Cambridge, MA, USA. [5]Department of Genetics, Harvard Medical School, Boston, MA, USA. [6]Wyss Institute for Biologically Inspired Engineering, Boston, MA, USA. [7]Department of Mechanical Engineering, University of California—Riverside, Riverside, CA, USA. [8]Center for the Development of Therapeutics, Broad Institute of MIT and Harvard, Cambridge, MA, USA. [9]Present address: School of Biopharmaceutical and Medical Sciences, Sungshin University, Seoul, South Korea. [10]These authors contributed equally: Donghyun Lim, Qingxuan Zhou, Kurt J. Cox, Benjamin K. Law, Miseon Lee, Praveen Kokkonda, Vedagopuram Sreekanth. ✉e-mail: achoudhary@bwh.harvard.edu

of anti-CRISPR molecules that can fine-tune nuclease activity over dose and time[6–8]. Ideal anti-CRISPR molecules should be: (1) cell-permeable for facile delivery, precise dosing and temporal control of the nuclease activity; (2) non-immunogenic and stable in circulation for in vivo use; (3) fast-acting to ensure rapid modulation of nuclease activity and specificity and (4) easy to use and inexpensive. Precision control of intracellular enzymes is nearly always accomplished using small molecules, which generally possess these desired attributes[9–11]. However, the identification of small-molecule inhibitors of CRISPR-associated nucleases requires a suite of robust, high-throughput, orthogonal, sensitive and inexpensive activity assays, which are currently unavailable. It is challenging to develop such assays because these nucleases operate via different mechanisms[12,13] and their tight binding to DNA yields a single turnover enzyme, preventing signal amplification via multiple catalytic cycles[14,15]. In addition, Cas nucleases possess two nuclease domains that would need to be inactivated and are DNA-binding proteins[12,16] that are often deemed chemically intractable. Finally, novel protein folds and massive conformational changes during the catalytic cycle complicate rational structure-guided design approaches[12,15,16].

We previously developed an assay to probe small molecules that disrupt the SpCas9–protospacer adjacent motif (PAM) interaction and discovered BRD0539, a first-generation SpCas9 inhibitor[17]. This small-molecule screening assay based on PAM recognition by SpCas9, the initial step in the catalytic process, overlooks other modes of inhibition (for example, nuclease activity) and requires high concentrations of SpCas9:guide RNA (gRNA) complex, both of which lower the chances of inhibitor discovery. Historically, assays that monitor protein:DNA interactions have not furnished potent small-molecule inhibitors[18]. In addition, different Cas nucleases recognize different PAM sequences, thereby preventing this assay from being generalizable to other Cas9 orthologues. Despite examining approximately 1,000 analogues, BRD0539 had poor potency, was unable to enhance SpCas9 specificity and its inhibitory activity depended on the genomic loci or mode of SpCas9 delivery (for example, plasmid or as a ribonucleoprotein (RNP) complex). Finally, BRD0539 synthesis is cumbersome (eight steps from commercially available materials) and low-yielding, which prohibits its optimization and large-scale production[17].

We hypothesized that small-molecule screening using an assay that cumulatively reports all steps of the catalytic cycle could furnish improved inhibitors. Here we describe such a fluorescence resonance energy transfer (FRET)-based cumulative activity assay (CAA) that reports on all of the catalytic activity steps, requires tenfold less SpCas9:gRNA complex compared with the PAM-binding assay and is broadly applicable across CRISPR nuclease families. Leveraging the high-throughput nature of the CAA, we screened 122,409 small molecules, followed by triaging with a suite of orthogonal cellular secondary assays. Using this pipeline, we discovered BRD7586, which is approximately twofold more potent than BRD0539 and inhibits SpCas9 at multiple genomic loci irrespective of the mode of SpCas9 delivery. We demonstrate that BRD7586 specifically engages SpCas9 but not Cas12a in cells and enhances SpCas9 specificity at multiple loci. With a molecular weight of 408 Da, BRD7586 is the smallest known anti-CRISPR and can be synthesized on a large scale in a single step from commercially available starting materials. Finally, based on structure–activity relationship studies, we have identified an inactive analogue of BRD7586. Overall, we present a general, inexpensive, high-throughput and ready-to-implement suite of assays to rapidly identify synthetic, miniature and cell-permeable inhibitors of CRISPR-associated nucleases and demonstrate the utility of the identified inhibitors to improve genome-editing specificity.

Results

Development of a CAA for SpCas9

We previously reported an assay that uses fluorescence polarization to monitor the binding between a fluorophore-labelled poly-PAM DNA oligonucleotide and SpCas9 charged with a non-targeting gRNA[17]. This assay permitted screening for small molecules that interfered with the early steps of the SpCas9 catalytic mechanism—that is, binding of SpCas9 and the relatively low-affinity NGG PAM DNA sequence. However, this assay failed to identify molecules that block the cutting activity of the nuclease domains of SpCas9 and could not be applied for Cas12a as the enzyme bound to the DNA in a PAM-independent fashion (Extended Data Fig. 1a–d). A high-throughput assay to monitor the nuclease activity of SpCas9 was reported but did not produce ideal chemical matter in terms of toxicity, potency and on-target specificity[19]. To address these issues, we sought to develop an assay that cumulatively reports on all steps in the catalytic cycle of these nucleases.

We based our assay on the observation that while Cas9 is bound to the DNA substrate following the double-strand break, the 5′ distal non-target DNA strand is only weakly held by Cas9 and this strand can be displaced following the addition of excess complementary single-stranded DNA (ssDNA)[14], analogous to toe-hold-mediated strand displacement[20,21]. Therefore, we designed a FRET-based assay wherein the 5′ end of the non-target strand in the substrate was labelled with a fluorophore. The 3′ end of the displacing ssDNA was labelled with a quencher. Following nuclease cleavage of the substrate, the 3′-labelled quenching DNA strand (present in excess) could outcompete the weakly held 3′ strand to anneal to the 5′ strand. The resulting FRET fluorescence quenching provides an optical readout for nuclease activity (Fig. 1a).

When we tested this CAA, loss of fluorescence was indeed only observed when active SpCas9:gRNA was added to a mixture of both the substrate and quencher. When all components were present, the quenching efficiency was similar to the control when the quencher was directly added to the complementary fluorophore-labelled single-strand oligonucleotide (Fig. 1b). We validated that the loss of fluorescence depended on the presence of an NGG PAM (Fig. 1c) and confirmed the activity correlation between the CAA and that observed using gel electrophoresis on the same assay (Fig. 1d). Importantly, CAA can recapitulate concentration-dependent inhibition of SpCas9 by anti-CRISPR proteins that operate through different mechanisms (Fig. 1e and Extended Data Fig. 1e). For example, AcrIIA4 disrupts the PAM recognition by the SpCas9:gRNA complex, whereas AcrIIA11 inhibits DNA cleavage by trapping SpCas9:gRNA at the PAM-rich sites[7,22–25]. However, CAA cannot distinguish between various inhibitory mechanisms, for which additional assays will be required.

Generalization of CAA to other Cas nucleases

We sought to generalize our CAA to other CRISPR-associated nucleases, including SaCas9. Given the similarities between the modes of DNA-substrate binding and protein folding of SaCas9 and SpCas9 (refs. [26,27]), we hypothesized that SaCas9-induced strand displacement could be similarly measured. Fluorescence quenching indeed correlated with substrate cleavage in our CAA with active SaCas9:gRNA and an ACGGGT PAM sequence, which was validated using gel electrophoresis (Fig. 1f,g and Extended Data Fig. 1f).

Next, we adapted the assay for other Cas-family enzymes, starting with Cas12a. There are several mechanistic differences between the Cas9 and Cas12a families, including the number of nuclease domains (Cas9 has two and Cas12a has one), orientation of substrate binding (Cas9 recognizes a 3′ PAM and Cas12a recognizes a 5′ PAM), and additional enzymatic functionalities (Cas12a undergo non-specific collateral DNase and RNase activity; Fig. 2a)[13,28–30]. To address these differences, we prepared Cas12a substrates containing a 3′ fluorophore on either the non-targeting (NTS-Fluor) or targeting strand (TS-Fluor; Fig. 2a). The NTS-Fluor substrate showed higher PAM-dependent quenching than the TS-Fluor substrate (Fig. 2b,c and Extended Data Fig. 2a,b), with the PAM-dependent cleavage observed in the CAA mirroring the gel electrophoresis results (Fig. 2d and Extended Data Fig. 2c). The CAA was able to report on concentration-dependent inhibition by AcrVA1

https://doi.org/10.1038/s41556-022-01005-8

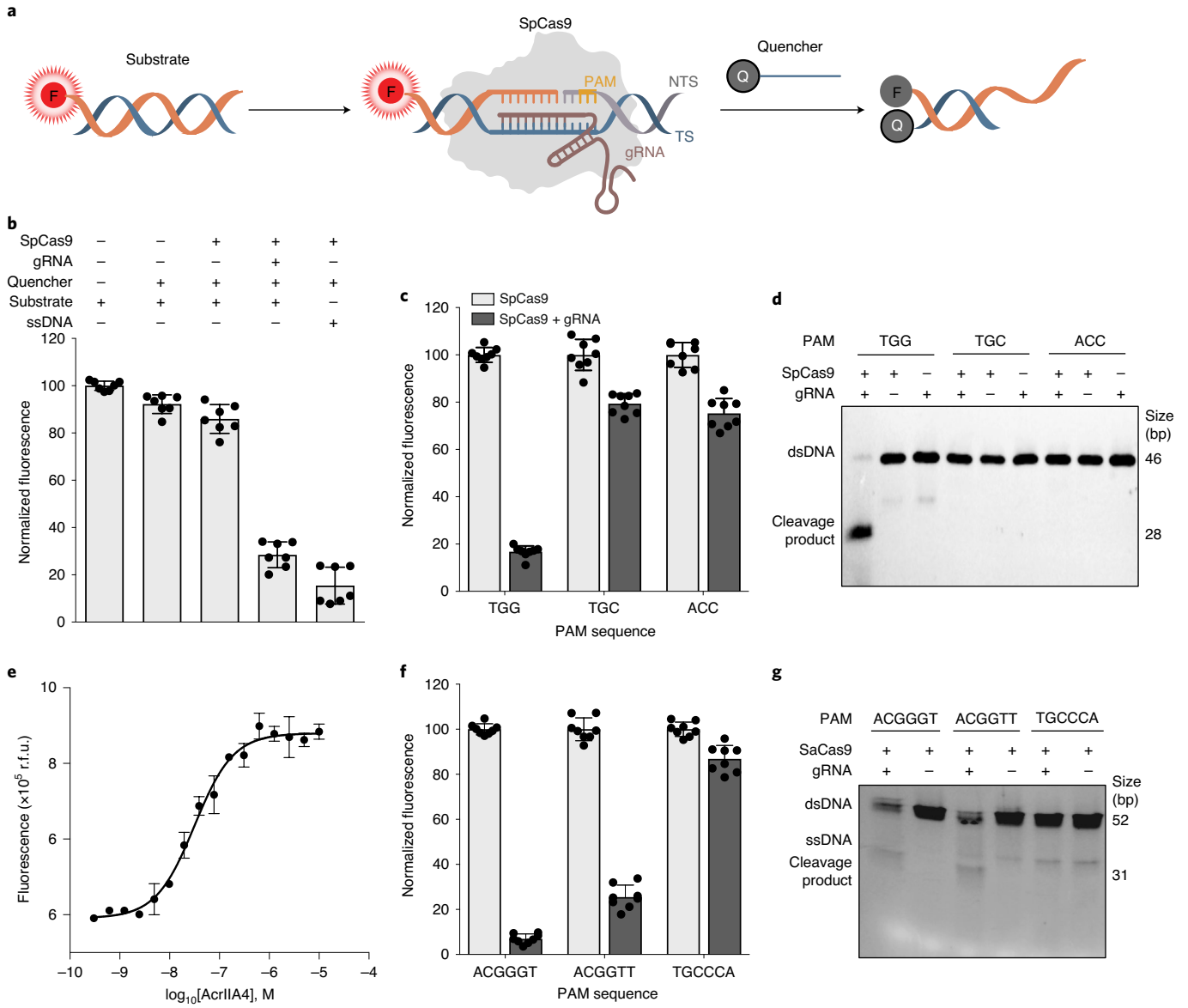

Fig. 1 | Development of the CAA. a, Schematic of the CAA . A double-stranded oligonucleotide containing a fluorophore (F) is cleaved by SpCas9. Following cleavage, the non-fluorophore-containing strand of the oligonucleotide substrate is displaced by a quencher (Q)-bearing oligonucleotide, decreasing the fluorescence signal through FRET. TS, targeting strand; and NTS, non-targeting strand. **b**, Demonstration of the SpCas9 CAA. The fluorescence of the SpCas9-specific substrate is not quenched in the presence of quencher unless the substrate is cleaved via an active SpCas9:gRNA complex. Fluorophore-tagged ssDNA can be completely quenched in the absence of an unlabelled complementary strand. Data are the mean ± s.d. of seven independent replicates. $P = 3.3 \times 10^{-10}$ for SpCas9:gRNA (4th bar) versus SpCas9 only (3rd bar); unpaired *t*-test, two-tailed. **c**, SpCas9 CAA with varying PAM sequences to demonstrate the assay specificity. For SpCas9:gRNA versus SpCas9, $P = 3.8 \times 10^{-18}$ (TGG PAM), 3.1×10^{-6} (TGC PAM) and 6.0×10^{-7} (ACC PAM); unpaired *t*-test, two-tailed. **d**, Gel-monitored cleavage of FAM-labelled oligonucleotides (20 nM) by the SpCas9:gRNA complex (100 nM) in a PAM-dependent manner. **e**, Inhibition of SpCas9 by AcrIIA4 at different concentrations, [AcrIIA4], monitored using the CAA . Data are the mean ± s.d. of three independent replicates. $P = 2.2 \times 10^{-5}$ for AcrIIA4 at 10 μM versus buffer only; unpaired *t*-test, two-tailed. **f**, SaCas9 CAA with varying PAM sequences to demonstrate the assay specificity. For SaCas9:gRNA versus SaCas9, $P = 3.9 \times 10^{-20}$ (ACGGGT PAM), 7.1×10^{-14} (ACGGTT PAM) and 8.5×10^{-5} (TGCCCA PAM); unpaired *t*-test, two-tailed. **c**,**f**, The light grey bars show results with SpCas9 only and the dark grey bars show results with the SpCas9:gRNA complex. Data are the mean ± s.d. of eight independent replicates. **g**, Gel-monitored cleavage of FAM-labelled oligonucleotides (20 nM) by the SaCas9:gRNA complex (100 nM) in a PAM-dependent manner. r.f.u., relative fluorescence units; dsDNA, double-stranded DNA.

but not AcrIIA4 (Fig. 2e), as reported previously[31]. Overall, these studies indicate the relative ease of generalizing CAA for different and emerging CRISPR-associated nucleases.

Optimization of CAA for high-throughput screening

To apply our CAA to high-throughput screening, it would need to sensitively detect SpCas9 activity within a reasonable time window. To minimize the interference from compound autofluorescence, we used a red-shifted Alexa Fluor 647-labelled double-stranded substrate (dsAF647) for assay development. The dsAF647 was readily detectable to as low as 1 nM and could be efficiently quenched by the complementary strand bearing the quencher (Disp-Q; Fig. 3a). We separately optimized the ratio of Disp-Q to 1 nM of dsAF647 and SpCas9:gRNA to 1 nM of dsAF647, and found that a fivefold excess of each reagent relative to

https://doi.org/10.1038/s41556-022-01005-8

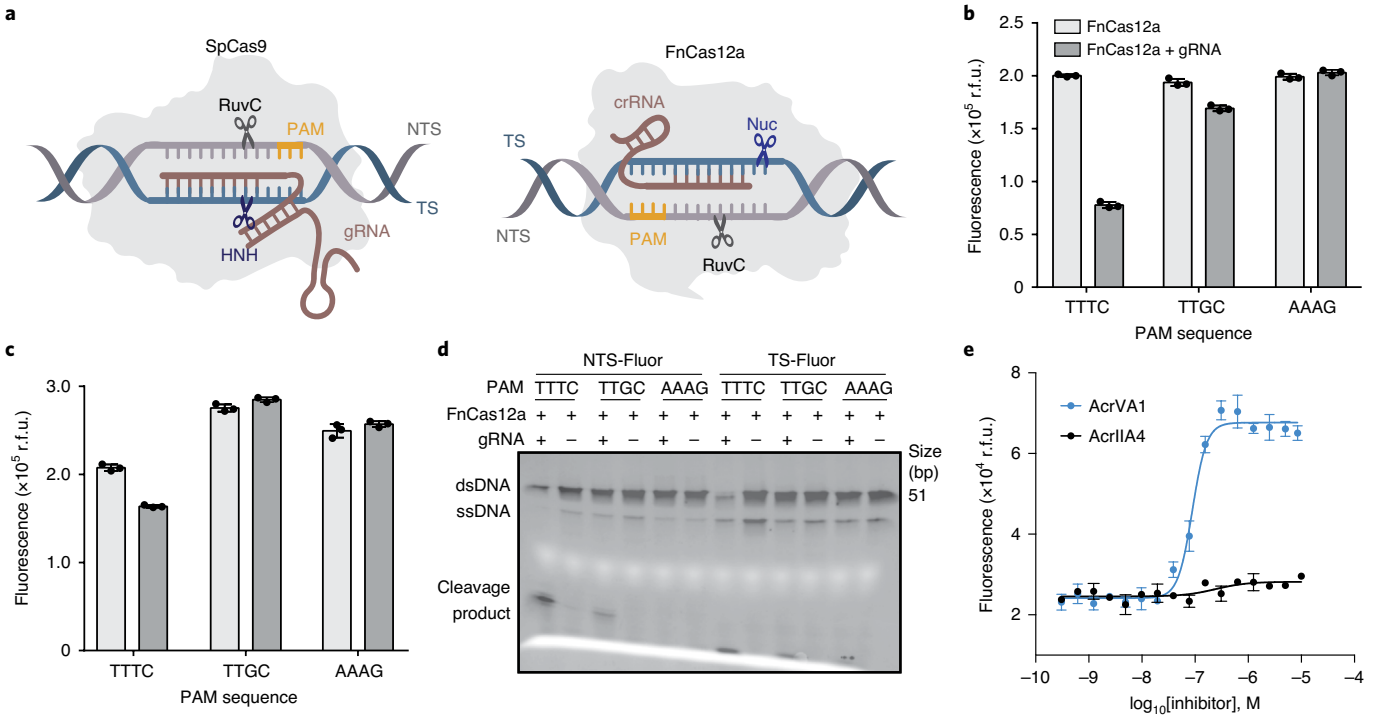

Fig. 2 | Generalization of the CAA to different Cas systems. a, Schematic of the substrate recognition by SpCas9 (left) and *Francisella novicida* Cas12a (FnCas12a; right). Cas12a enzymes bind DNA in a reverse orientation compared with Cas9. Generalization of the CAA to Cas12a enzymes requires optimization of the location of the fluorophore on either the non-targeting (NTS) or targeting (TS) strand. crRNA, *crispr* RNA. **b**, FnCas12a CAA with varying PAM sequences using an NTS-labelled fluorophore. For FnCas12a:gRNA versus FnCas12a, $P = 2.8 \times 10^{-7}$ (TTTC PAM), 6.4×10^{-4} (TTGC PAM) and 0.15 (AAAG PAM); unpaired *t*-test, two-tailed. **c**, FnCas12a CAA with varying PAM sequences using TS-Fluor. For FnCas12a:gRNA versus FnCas12a, $P = 4.5 \times 10^{-5}$ (TTTC PAM), 0.030 (TTGC PAM) and 0.19 (AAAG PAM); unpaired *t*-test, two-tailed. **b**,**c**, The light grey bars show results with FnCas12a only and the dark grey bars show results with the FnCas12a:gRNA complex. **d**, Gel-monitored cleavage of the FAM-labelled oligonucleotides NTS-Fluor and TS-Fluor (100 nM) by FnCas12a (500 nM). **e**, Inhibition of FnCas12a by two anti-CRISPR proteins, AcrIIA4 and AcrVA1, monitored using the CAA. $P = 5.4 \times 10^{-6}$ (AcrVA1 at 5 μM compared with buffer only) and 0.16 (AcrIIA4 at 5 μM compared with buffer only); unpaired *t*-test, two-tailed. **b**,**c**,**e**, Data are the mean ± s.d. of three independent replicates; r.f.u., relative fluorescence units.

dsAF647 yielded maximum quenching (Fig. 3b,c). A time-course study of fluorescence quenching at various SpCas9:gRNA and dsAF647 ratios revealed that the reaction was effectively completed after 2.5 h (Fig. 3d). After adapting the assay for liquid handling systems to enable high-throughput screening, we were able to detect 5 nM SpCas9 using 0.5 nM dsAF647 with a *Z′* factor (reports on the degree of separation between positive and negative control[32]) of 0.72 (Fig. 3e).

Primary and secondary screening

Our primary screen assayed a selection of unique chemical scaffolds derived from commercially available compounds and known bioactive molecular libraries (Supplementary Table 1). Autofluorescent compounds were removed by a counter screen. Overall, the CAA was used to assay 122,409 small molecules with over 2,500 unique chemical scaffolds (Fig. 3f and Supplementary Table 1). Of these compounds, 547 were selected as hits (*Z* score > 3 in both replicates) for testing in orthogonal cell-based secondary assays. These hits were tested in duplicate in an *eGFP*-disruption assay, wherein U2OS.eGFP.PEST cells[33] transfected with SpCas9 plasmid and *eGFP*-targeting gRNA plasmid were incubated with 20 μM of the compounds. In this assay, any compound that inhibited SpCas9 would rescue the loss of eGFP fluorescence. Here toxic and autofluorescent compounds with a high GFP signal in cells were removed as false positives. Of the 547 compounds tested in cellular assays, 15 had a *Z* score of >2 and 11 had a *Z* score of >3 in two independent screens (Fig. 3g). Next, we tested the 15 compounds in a luminescence-based gain-of-signal *HiBiT*-knock-in assay, which involves SpCas9-mediated homology-directed tagging of GAPDH with a short peptide that luminesces on complementation with a subunit derived from nanoluciferase[34]. Complementarily, the *eGFP*-disruption assay is fluorescence-based and involves error-prone DNA repair. As a counter screen to remove false positives caused by cell death (viability < 80%), the cell viability was measured after incubation. Interestingly, the top three-performing compounds had a similar core structure, so we selected BRD7586 for further studies. Furthermore, BRD7586 exhibited higher potency than BRD0539 in the *HiBiT*-knock-in assay (Fig. 3h,i and Extended Data Fig. 3a), and we confirmed dose-dependent inhibition of SpCas9 by BRD7586 in CAA (Extended Data Fig. 3b) and in vitro DNA cleavage (Extended Data Fig. 3c,d) assays.

Cellular activities of BRD7586

We next confirmed dose-dependent inhibition of SpCas9 by BRD7586 in multiple assays with an orthogonal readout (for example, fluorescence, luminescence and next-generation sequencing) and at multiple genomic loci. The half maximal effective concentrations of BRD7586 in the *eGFP*-disruption and *HiBiT*-knock-in assays (three independent experiments) were 6.2 ± 1.2 μM and 5.7 ± 0.36 μM, respectively, which are lower than our first-generation inhibitor BRD0539 at approximately 12 μM (Fig. 4a–c). More importantly, BRD7586 inhibited the indel activity of SpCas9 at multiple genomic loci, as determined using next-generation sequencing (Fig. 4d,e and Extended Data Fig. 4a,b). Furthermore, BRD7586 enhanced the specificity of SpCas9. HEK293T cells were transfected with SpCas9 and gRNA plasmids targeting the genes *EMX1*, *FANCF* or *VEGFA* and then incubated with BRD7586 for 48 h. Here we observed the enhanced on-target versus off-target ratio with an

https://doi.org/10.1038/s41556-022-01005-8

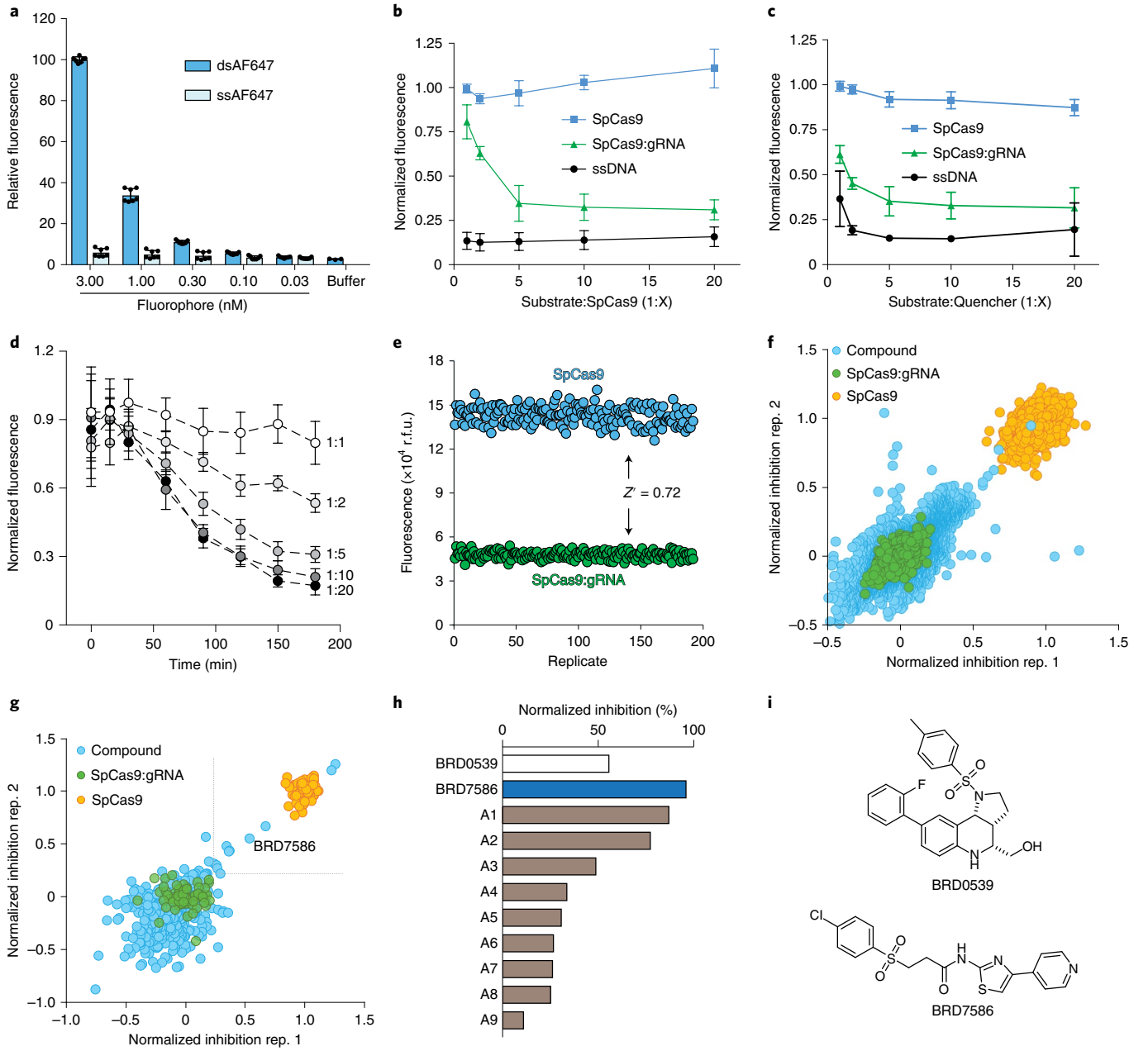

Fig. 3 | High-throughput optimization and screening with the CAA. **a**, Optimization of the double-stranded substrate (dsAF647) concentration relative to single-stranded substrate (ssAF647) fully quenched by binding to Disp-Q. $P = 1.1 \times 10^{-10}$ for ssAF647 versus dsAF647 at 1 nM; unpaired *t*-test, two-tailed. **b**, Optimization of the relative ratio of SpCas9:gRNA (1–20 nM) to dsAF647 (1 nM) with fixed Disp-Q (5 nM). $P = 1.6 \times 10^{-8}$ for SpCas9:gRNA versus SpCas9 at a substrate:SpCas9 ratio of 1:5; unpaired *t*-test, two-tailed. **c**, Optimization of the relative ratio of Disp-Q (1–20 nM) to dsAF647 (1 nM) with fixed SpCas9:gRNA (5 nM). $P = 1.5 \times 10^{-9}$ for SpCas9:gRNA compared with SpCas9 at a substrate:Disp-Q ratio of 1:5; unpaired *t*-test, two-tailed. **a**–**c**, Data are the mean ± s.d. of seven independent replicates. **d**, DNA cleavage over time with varying amounts of SpCas9:gRNA and fixed dsAF647 (1 nM). Data are the mean ± s.d. of three independent replicates. $P = 0.0128$ for 150 min versus 0 min for a substrate-to-SpCas9 RNP ratio of 1:5; unpaired *t*-test, two-tailed. **e**, High-throughput validation of the CAA using 10 nM SpCas9:gRNA (1:1.2) or 10 nM SpCas9 (25 µl) distributed in a 384-well plate, followed by the addition of 1 nM dsAF647 and 5 nM Disp-Q (25 µl). **f**, High-throughput screening against 122,409 compounds performed in duplicate. To compare results from different screening plates, the *Z* scores from each compound were normalized by setting the dimethylsulfoxide (DMSO) control as zero and SpCas9 without gRNA as one. **g**, Secondary screening of 547 hit compounds using an *eGFP*-disruption assay. The screen was performed in duplicate and normalized as in **f**. Blue dots at the right and above of the grey lines are for compounds with a *Z* score of >3 in both independent experiments. **h**, SpCas9 inhibition by hit compounds in a tertiary *HiBiT*-knock-in assay. The empty box represents the BRD0539 positive control, the coloured boxes represent hit compounds. **i**, Structures of BRD7586 (bottom) and the reported SpCas9 inhibitor BRD0539 (top).

increasing amount of inhibitor (Fig. 4f). Moreover, BRD7586 exhibited substantially improved activity compared with first-generation BRD0539 (ref. [17]) in the *eGFP*-disruption and *HiBiT*-knock-in assays (Extended Data Fig. 4c,d).

BRD7586 inhibited SpCas9 in both HEK293T and U2OS.eGFP.PEST cells without altering its expression (Fig. 4g and Extended Data Fig. 5a,b), introducing cytotoxicity (Fig. 4h) or affecting the eGFP expression in U2OS.eGFP.PEST cells in the absence of SpCas9:gRNA

https://doi.org/10.1038/s41556-022-01005-8

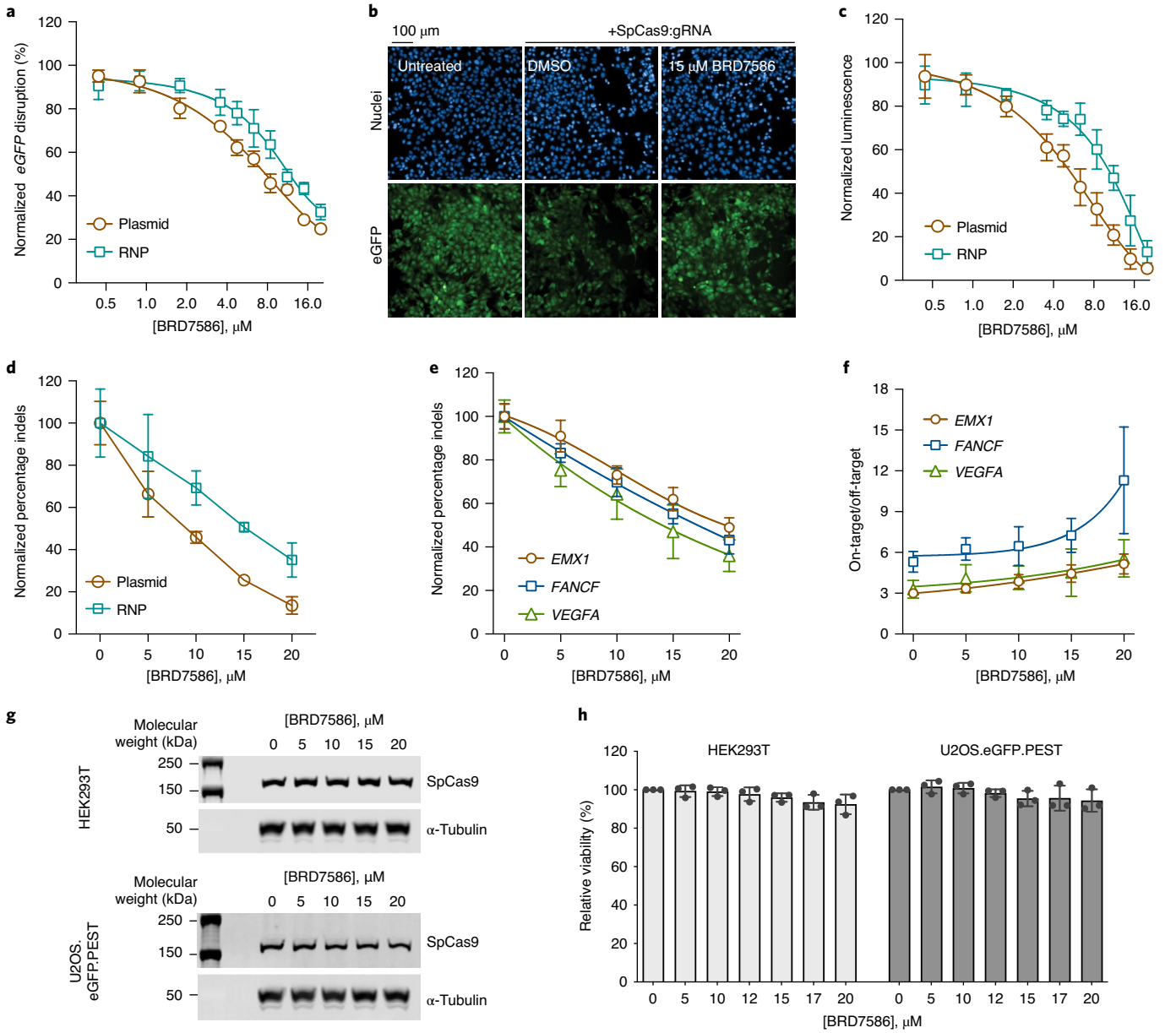

Fig. 4 | Cellular validation of BRD7586. a, Dose-dependent inhibition of SpCas9 by BRD7586 in an *eGFP*-disruption assay using plasmid and RNP delivery methods. For 20 μM BRD7586 versus DMSO, $P = 2.6 \times 10^{-9}$ (plasmid delivery) and 1.9×10^{-7} (RNP delivery); unpaired *t*-test, two-tailed. **b**, Inhibition of *eGFP*-targeting SpCas9 by BRD7586 in U2OS.eGFP.PEST cells nucleofected with RNP (24 h). **c**, Dose-dependent SpCas9 inhibition by BRD7586 in the *HiBiT*-knock-in assay in HEK293T cells (24 h). For 20 μM BRD7586 versus DMSO, $P = 6.2 \times 10^{-12}$ (plasmid delivery) and 9.0×10^{-10} (RNP delivery). **a**,**c**, Data are the mean ± s.d. of six independent replicates. **d**, Dose-dependent inhibition of *eGFP*-targeting SpCas9 measured through deep sequencing. U2OS.eGFP.PEST cells were nucleofected with plasmids or RNP and incubated with BRD7586 (24 h). Data are the mean ± s.d. of four independent replicates. For 20 μM BRD7586 versus DMSO, $P = 4.3 \times 10^{-6}$ (plasmid) and 3.7×10^{-4} (RNP). **e**, Dose-dependent inhibition of SpCas9 targeting *EMX1*, *FANCF* or *VEGFA*. HEK293T cells were transfected with plasmids and incubated with BRD7586 (24 h). Data are the mean ± s.d. of seven (*EMX1*) and six (*FANCF* and *VEGFA*) independent replicates. For 20 μM BRD7586 versus DMSO, $P = 3.9 \times 10^{-10}$ (*EMX1*), 1.7×10^{-8} (*FANCF*) and 3.8×10^{-8} (*VEGFA*). **f**, Effect of BRD7586 on the specificity of SpCas9. HEK293T cells were transfected with plasmids and incubated with BRD7586 (48 h). Data are the mean ± s.d. of seven independent replicates. Specificity was calculated as a ratio of normalized indel frequencies. For 20 μM BRD7586 versus DMSO, $P = 9.1 \times 10^{-6}$ (*EMX1*), 0.0019 (*FANCF*) and 0.0019 (*VEGFA*). **g**, Immunoblots to assess SpCas9 expression in cells transfected with SpCas9 plasmid and incubated with BRD7586 (24 h). **h**, Viability of cells incubated with BRD7586, measured using CellTiter-Glo (24 h). Data are the mean ± s.d. of three independent replicates. For 20 μM BRD7586 versus DMSO, $P = 0.062$ (HEK293T cells) and 0.17 (U2OS.eGFP.PEST). [BRD7586], concentration of BRD7586.

(Extended Data Fig. 5c). Although BRD7586 inhibited SpCas9, it did not affect the activity of structurally distinct Cas12a from *Lachnospiraceae bacterium* (LbCas12a), demonstrating its nuclease-selective activity (Extended Data Fig. 5d). Finally, BRD7586 was 40% stable in mouse plasma.

Structure–activity relationship studies of BRD7586

To identify the pharmacophore of the molecular scaffold, we performed structure–activity relationship (SAR) studies of BRD7586. We assembled analogues by individually substituting the R^1 and R^2 positions with different chemical functional groups (Fig. 5a) and tested these

https://doi.org/10.1038/s41556-022-01005-8

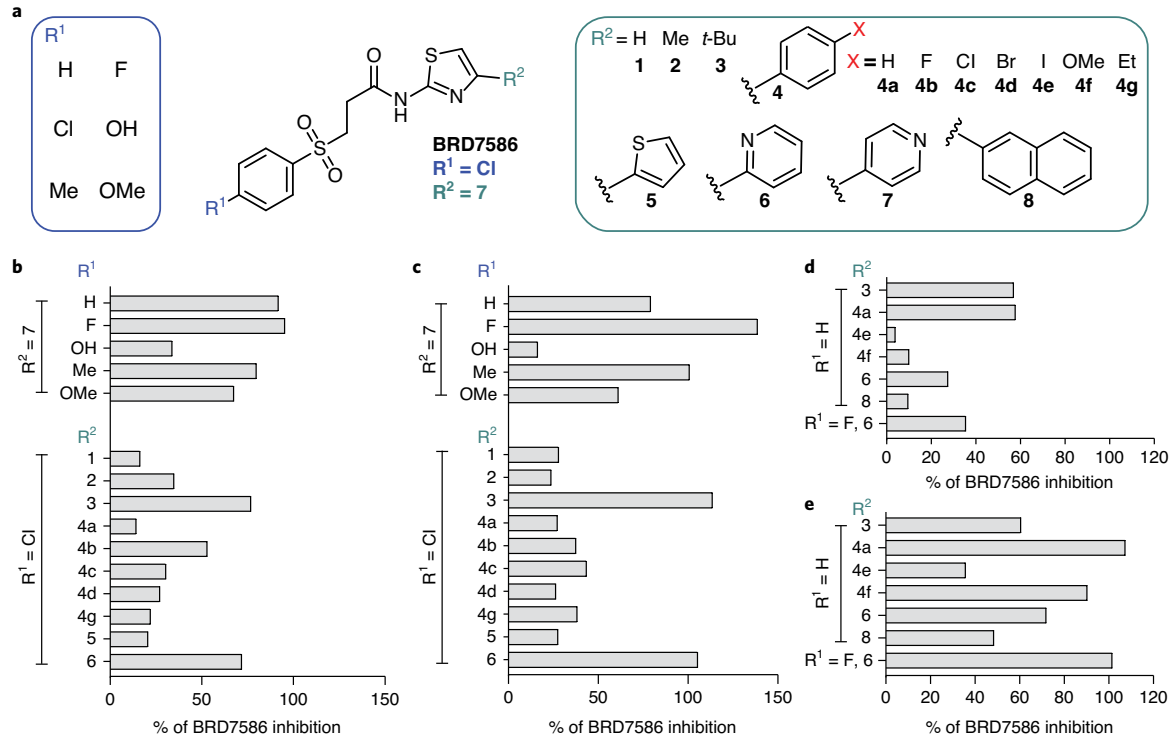

Fig. 5 | Structure–activity relationship studies with BRD7586. a, Structure of the compounds used for the SAR studies. The left box represents substitutions around the phenyl ring (R^1) and the right box represents variation of the thiazole endcap (R^2). **b**, Structure–activity relationship studies (single modification) in the *eGFP*-disruption assay in comparison to BRD7586. **c**) Structure–activity relationship studies (single modification) in the *HiBiT*-knock-in assay in comparison to BRD7586. **d**, Structure–activity relationship studies (double modification) in the *eGFP*-assay in comparison to BRD7586. **e**, Structure–activity relationship studies (double modification) in the *HiBiT*-knock-in assay in comparison to BRD7586.

analogues in both *eGFP*-disruption (Fig. 5b) and *HiBiT*-knock-in (Fig. 5c) assays. Keeping R^1 = Cl and varying R^2 substantially changed the SpCas9 activity from the eGFP-disruption assay. First, replacement of the pyridyl group (R^2 = 6, 7) with phenyl rings (R^2 = 4a, 4b, 4c, 4d, 4g), a 2-thienyl group (R^2 = 5) or smaller substituents such as hydrogen (R^2 = 1) or a methyl group (R^2 = 2) greatly decreased the activity. Instead, replacement of the pyridyl ring with a tert-butyl group (R^2 = 3) only slightly decreased the activity. Keeping R^2 = 7 and varying R^1 only slightly impacted the activity, with the exception of the hydroxyl substitution. These compounds were tested in the *HiBiT*-knock-in assay by incubating 15 µM of each analogue with HEK293T cells transfected with SpCas9:gRNA ribonucleoprotein (RNP) for 24 h (Fig. 5c). Similar trends were observed in this orthogonal assay, except that a higher apparent activity was observed in a few compounds that also exhibited slight toxicity in this assay.

In addition to single modifications, we examined double modifications of BRD7586. These analogues were also tested using *eGFP*-disruption (Fig. 5d) and *HiBiT*-knock-in (Fig. 5e) assays and demonstrated similar trends to the individual substitutions, indicating that the opposite handles of the compound act to stabilize the pocket independently. Once again, the *HiBiT*-knock-in assay displayed higher inhibition than observed in the *eGFP*-disruption assay, although we observed some toxicity that resulted in a higher apparent activity.

Biochemical activity of BRD7586

Similar to the cellular studies, we characterized the activity and binding of BRD7586 to SpCas9 using orthogonal readouts (for example, NMR and biolayer interferometry). We used saturation transfer difference (STD) NMR to probe the binding of 20 µM BRD7586 to 5 µM of the SpCas9:gRNA complex. We observed STD NMR signal from marked protons, suggesting that these are directly involved in binding to the SpCas9 complex (Fig. 6a). The same STD NMR experiment in the absence of protein did not display a STD NMR signal, suggesting that the signal does not arise from aggregation or other artefacts. The STD NMR suggests that there is an interaction between SpCas9 and the phenyl-group protons, the thiazole proton and the protons adjacent to the nitrogen on the pyridyl ring but not with the other protons.

Based on the SAR and STD NMR studies, we identified the para position of the phenyl ring as a probable tolerable linker attachment site on BRD7586 (Fig. 5). In addition, the STD NMR and SAR studies indicated that the pyridine group was involved in the binding and would thus not tolerate any substitutions. We attached a biotin-PEG3 to the para position of the phenyl ring to synthesize biotin-BRD7586 (Extended Data Fig. 6a). Biolayer interferometry studies using 1 µM biotin-BRD7586 with SpCas9:gRNA complex suggested a dissociation constant of 0.52 µM (Fig. 6b,c). No detectable binding was observed when the SpCas9:gRNA complex was added to biotin-PEG3-azide in the absence of the BRD7586 parent scaffold (Extended Data Fig. 6b).

Target engagement and design of inactive analogue

We used a photo-affinity labelling strategy to demonstrate target engagement in cells via a diazirine-based BRD7586 (Fig. 7a)[35–37]. Based on the SAR studies, we designed and synthesized a photo-crosslinking probe (diazirine-BRD7586) bearing a minimalist tag containing a photoreactive diazirine moiety and alkyne handle. The probe inhibited SpCas9 in cells, in accordance with the SAR results (Extended Data Fig. 7a). To establish crosslinking of diazirine-BRD7586 to its target, SpCas9:gRNA complex was incubated with diazirine-BRD7586 and the mixture was photo-irradiated. Click chemistry with TAMRA-azide allowed the visualization of the crosslinking product through in-gel fluorescence analysis. We demonstrated successful covalent conjugation of the probe to SpCas9. Furthermore, the crosslinking was

https://doi.org/10.1038/s41556-022-01005-8

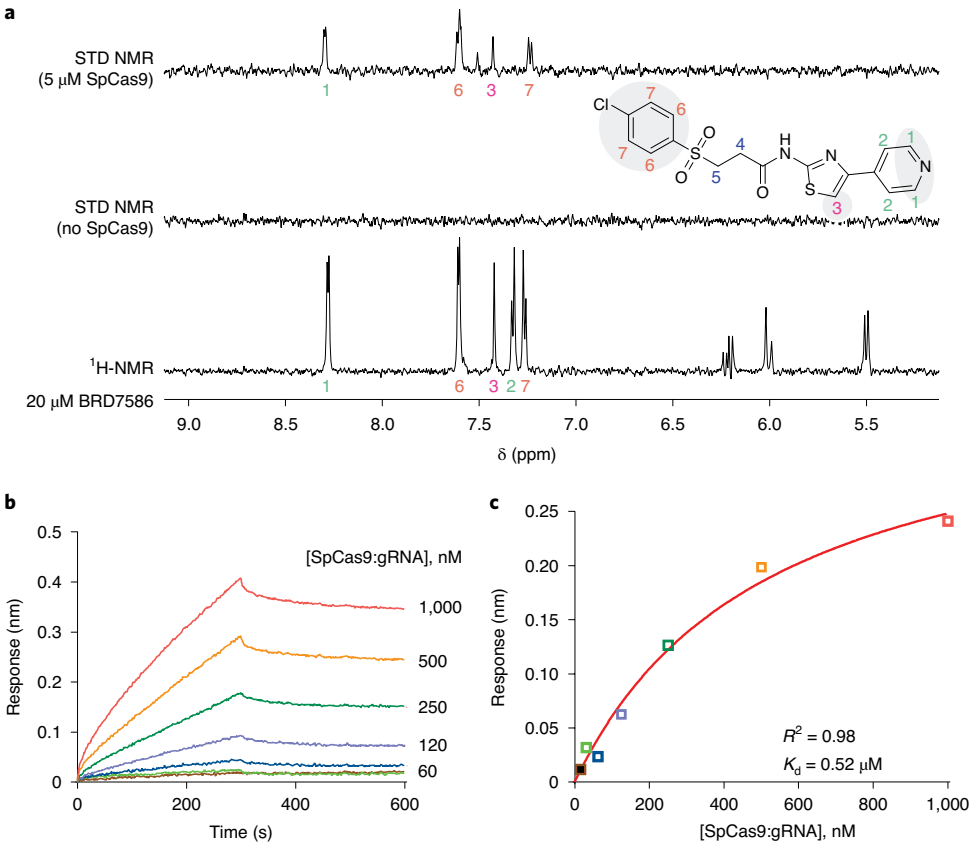

Fig. 6 | Biochemical binding studies of BRD7586. a, Saturation transfer difference NMR of 20 μM BRD7586 with and without 5 μM SpCas9:gRNA complex. The STD NMR signal was obtained through subtraction of NMR signal with and without STD magnetization signal. **b**, Biolayer interferometry (BLI) binding plot for biotin-BRD7586 and SpCas9:gRNA complex. The BLI experiment was performed using 1 μM biotin-BRD7586 on streptavidin sensors, followed by association with different concentrations of the SpCas9:gRNA complex (indicated on the right) and subsequent dissociation. **c**, Steady-state analysis of the BLI binding results to determine the dissociation constant (K_d). A global model was used to plot the steady state and determine the binding constant. R^2, squared coefficient of multiple correlation.

selective, as demonstrated via competition with BRD7586 (Fig. 7b). We then validated target engagement of BRD7586 via photo-irradiation in live cells treated with diazirine-BRD7586 in the presence and absence of BRD7586. After cell lysis and click chemistry with biotin-azide, the crosslinked proteins were enriched using streptavidin pulldown and immunoblotting to reveal the formation of crosslinks between diazirine-BRD7586 and SpCas9 (Extended Data Fig. 7b). This binding was abolished in the presence of BRD7586 as a competitor, demonstrating target engagement in live cells (Fig. 7c).

Based on SAR studies, we designed an inactive analogue of BRD7586 containing a bulky bromophenyl group and thioether that can serve as a control. This analogue (BRD0033) was inactive in both the *eGFP*-disruption and *HiBiT*-knock-in assays (Fig. 7a,d,e). In addition, another analogue (F2537-0908) containing a thioether linkage instead of the sulfonyl group, but with the other substituent unchanged from BRD7586, had substantially lower inhibitory activity in both the *eGFP*-disruption and *HiBiT*-knock-in assays (Extended Data Fig. 8a–c).

Finally, we performed early studies towards understanding the molecular mechanism of inhibition. Our previously reported SpCas9:PAM interaction assay[17] showed that BRD7586 does not inhibit binding between the SpCas9:gRNA complex and DNA (Extended Data Fig. 8d), further suggesting that BRD7586 potentially disrupts SpCas9 catalysis. We also performed early studies towards binding pocket identification using photo-crosslinked SpCas9:gRNA and diazirine-BRD7586, after which an acid-cleavable and isotope-coded biotin-azide (Extended Data Fig. 7c) was appended to the conjugate via click chemistry (Extended Data Fig. 7b). Streptavidin pulldown, followed by tryptic digestion left only the crosslinked peptides on the bead surface and acid-mediated cleavage released the crosslinked peptides with the unique isotope tag identified using mass spectrometry (Extended Data Fig. 7d). After confirming the isotope patterns using mass spectrometry, we identified peptides that crosslinked with BRD7586 (Extended Data Fig. 7e,f and Supplementary Table 8). We also performed docking studies using Schrödinger Maestro v12.1 in the region of the photo-crosslinked sites (Protein Data Bank, 5F9R)[38]. These results suggest that the inhibitor may bind between the HNH nuclease and the helical recognition domains (Extended Data Fig. 7g), although additional studies are needed to experimentally confirm these computational results.

Discussion

Here we report a universal platform to identify inhibitors of CRISPR-associated nucleases and demonstrate its usefulness by identifying a potent small-molecule inhibitor of SpCas9. Addressing issues in previous assay formats that bottlenecked the inhibitor discovery process, our platform is broadly applicable across multiple nuclease families and can report on the inhibition of any stage in the catalytic process. For example, our CAA for CRISPR-associated nucleases enabled the interrogation of all aspects of catalysis such as DNA binding, protein conformational changes and DNA cleavage, allowing a higher chance of inhibitor discovery. Furthermore, CAA can be used for both Cas9 and Cas12a despite the fact that they have a relatively different

https://doi.org/10.1038/s41556-022-01005-8

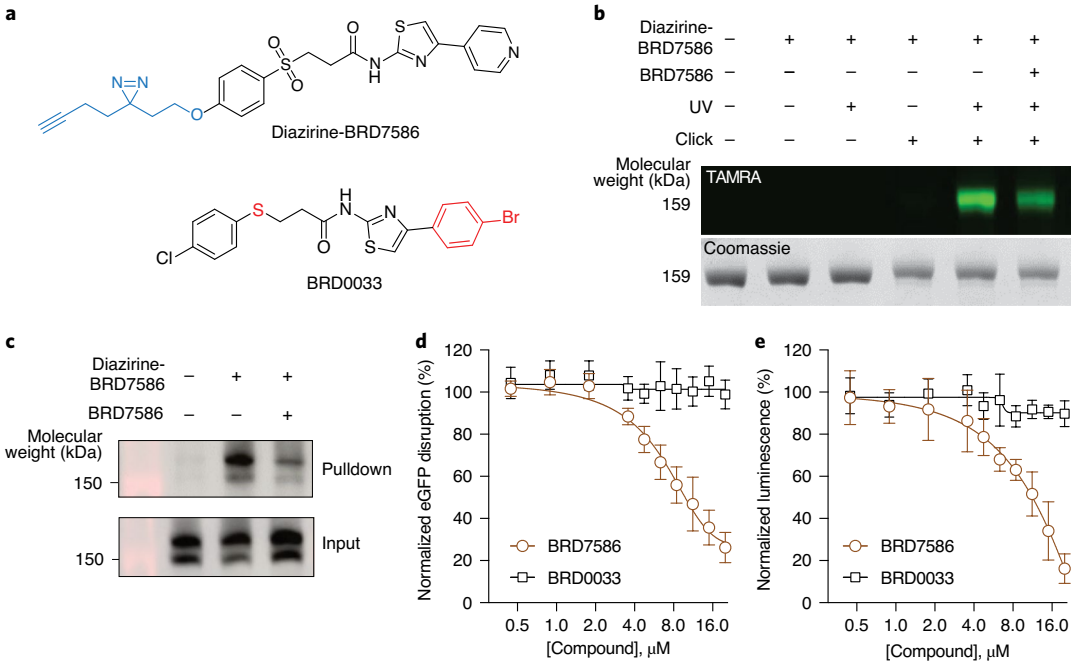

Fig. 7 | BRD7586 mechanism-of-action studies. a, Chemical structures of diazirine-BRD7586 (top) and an inactive analogue, BRD0033 (bottom). Substitutions from the parent compound (BRD7586) are labelled in blue (diazirine-BRD7586) and red (BRD0033). **b**, Engagement of BRD7586 to purified SpCas9. Diazirine-BRD7586 (1 μM) was photo-crosslinked to SpCas9:gRNA (1 μM) and tagged with TAMRA-azide through click chemistry. TAMRA fluorescence was detected only in the presence of ultraviolet light (UV), click chemistry reagents and diazirine-BRD7586. Competition with BRD7586 (5 μM) resulted in decreased photo-crosslinking. **c**, Target engagement of BRD7586 in live cells. HEK293T cells transiently expressing Cas9 were treated with diazirine-BRD7586, followed by in-cell photo-crosslinking. Cells lysis and click chemistry tagged the diazirine-BRD7586-bound proteins with biotin, which were pulled down by streptavidin beads and probed for the presence of SpCas9 by immunoblotting. **d**, Activity of BRD0033 and BRD7586 in an *eGFP*-disruption assay. For 20 μM compound versus DMSO, $P = 0.27$ (BRD0033) and 3.2×10^{-9} (BRD7586); unpaired *t*-test, two-tailed. **e**, Activity of BRD0033 and BRD7586 in the *HiBiT*-knock-in assay. For 20 μM compound versus DMSO, $P = 0.047$ (BRD0033) and 4.5×10^{-9} (BRD7586); unpaired *t*-test, two-tailed. **d**,**e**, Data are the mean ± s.d. of six independent replicates.

mode of catalysis, and we expect that CAA would be readily adapted for emerging CRISPR-associated nucleases. Logical computation capabilities can be added to the CAA set-up using DNA logic circuits[39,40]. We also demonstrate a robust and rapid workflow to verify cellular activities of numerous hits from the CAA, which involves a fluorescence imaging-based *eGFP*-disruption assay and a luminescence-based *HiBiT*-knock-in assay. Because these high-throughput assays are completely orthogonal, our platform allows for reliable identification of the final lead compound with minimal resources and time.

A potent small-molecule inhibitor of SpCas9 identified from our workflow, BRD7586, exhibited inhibitory activity in all explored genome-editing scenarios. In particular, BRD7586 inhibited genome editing at diverse endogenous loci regardless of the delivery methods of the genome-editing machinery (that is, plasmid or RNP). Moreover, treatment with BRD7586 improved the specificity of genome editing at diverse genomic loci, demonstrating its immediate usefulness for precise genome editing. As small molecules are readily cell-permeable, BRD7586 will complement anti-CRISPR proteins in therapeutic genome editing. The specific nature of the interaction between BRD7586 and the SpCas9 RNP complex was demonstrated using SAR studies. Whereas BRD0539 possesses a complex tetrahydroquinoline core requiring eight synthetic steps, several of which are challenging[17], BRD7586 possesses a simple core that can be accessed in a single step from commercially available materials. Owing to ease of synthesis, we envision that BRD7586 could serve as a starting point for more potent inhibitors and degraders of SpCas9 (refs. [41,42]). For example, proteolysis-targeting chimaeras[41,42] could be generated by joining our inhibitor to the ubiquitin ligase binder to cause the degradation of SpCas9. Overall, our reported anti-CRISPR molecules highlight that chemical approaches can control and enhance the capabilities of CRISPR-based technologies and are an important step towards their dose and temporal control. These studies have the potential to impact wide-ranging areas in basic and biomedical sciences and biotechnology.

Online content

Any methods, additional references, Nature Research reporting summaries, source data, extended data, supplementary information, acknowledgements, peer review information; details of author contributions and competing interests; and statements of data and code availability are available at https://doi.org/10.1038/s41556-022-01005-8.

References

1. Fellmann, C., Gowen, B. G., Lin, P. C., Doudna, J. A. & Corn, J. E. Cornerstones of CRISPR–Cas in drug discovery and therapy. *Nat. Rev. Drug Discov.* **16**, 89–100 (2017).
2. Gangopadhyay, S. A. et al. Precision control of CRISPR–Cas9 using small molecules and light. *Biochemistry* **58**, 234–244 (2019).
3. Kang, S.H. et al. Prediction-based highly sensitive CRISPR off-target validation using target-specific DNA enrichment. *Nat. Commun.* **11**, 3596 (2020).
4. Cox, D. B. T., Platt, R. J. & Zhang, F. Therapeutic genome editing: prospects and challenges. *Nat. Med.* **21**, 121–131 (2015).
5. Modell, A. E., Siriwardena, S. U., Shoba, V. M., Li, X. & Choudhary, A. Chemical and optical control of CRISPR-associated nucleases. *Curr. Opin. Chem. Biol.* **60**, 113–121 (2020).
6. Davidson, A. R. et al. Anti-CRISPRs: protein inhibitors of CRISPR-Cas systems. *Annu. Rev. Biochem.* **89**, 309–332 (2020).
7. Marino, N. D., Pinilla-Redondo, R., Csorgo, B. & Bondy-Denomy, J. Anti-CRISPR protein applications: natural brakes for CRISPR–Cas technologies. *Nat. Methods* **17**, 471–479 (2020).

8. Yu, L. & Marchisio, M. A. Types I and V anti-CRISPR proteins: from phage defense to eukaryotic synthetic gene circuits. *Front. Bioeng. Biotechnol.* **8**, 575393 (2020).
9. O'Connor, C. J., Laraia, L. & Spring, D. R. Chemical genetics. *Chem. Soc. Rev.* **40**, 4332–4345 (2011).
10. Walsh, D. P. & Chang, Y. T. Chemical genetics. *Chem. Rev.* **106**, 2476–2530 (2006).
11. Burslem, G. M. & Crews, C. M. Small-molecule modulation of protein homeostasis. *Chem. Rev.* **117**, 11269–11301 (2017).
12. Jiang, F. & Doudna, J. A. CRISPR–Cas9 structures and mechanisms. *Annu. Rev. Biophys.* **46**, 505–529 (2017).
13. Stella, S., Alcon, P. & Montoya, G. Structure of the Cpf1 endonuclease R-loop complex after target DNA cleavage. *Nature* **546**, 559–563 (2017).
14. Richardson, C. D., Ray, G. J., DeWitt, M. A., Curie, G. L. & Corn, J. E. Enhancing homology-directed genome editing by catalytically active and inactive CRISPR–Cas9 using asymmetric donor DNA. *Nat. Biotechnol.* **34**, 339–344 (2016).
15. Zhu, X. et al. Cryo-EM structures reveal coordinated domain motions that govern DNA cleavage by Cas9. *Nat. Struct. Mol. Biol.* **26**, 679–685 (2019).
16. Huai, C. et al. Structural insights into DNA cleavage activation of CRISPR–Cas9 system. *Nat. Commun.* **8**, 1375 (2017).
17. Maji, B. et al. A high-throughput platform to identify small-molecule inhibitors of CRISPR–Cas9. *Cell* **177**, 1067–1079 (2019).
18. Koehler, A. N. A complex task? Direct modulation of transcription factors with small molecules. *Curr. Opin. Chem. Biol.* **14**, 331–340 (2010).
19. Seamon, K. J., Light, Y. K., Saada, E. A., Schoeniger, J. S. & Harmon, B. Versatile high-throughput fluorescence assay for monitoring Cas9 activity. *Anal. Chem.* **90**, 6913–6921 (2018).
20. Yurke, B., Turberfield, A. J., Mills, A. P. Jr., Simmel, F. C. & Neumann, J. L. A DNA-fuelled molecular machine made of DNA. *Nature* **406**, 605–608 (2000).
21. Srinivas, N. et al. On the biophysics and kinetics of toehold-mediated DNA strand displacement. *Nucleic Acids Res.* **41**, 10641–10658 (2013).
22. Dong, D. et al. Structural basis of CRISPR–SpyCas9 inhibition by an anti-CRISPR protein. *Nature* **546**, 436–439 (2017).
23. Yang, H. & Patel, D. J. Inhibition mechanism of an anti-CRISPR suppressor AcrIIA4 targeting SpyCas9. *Mol. Cell* **67**, 117–127 (2017).
24. Forsberg, K. J. et al. Functional metagenomics-guided discovery of potent Cas9 inhibitors in the human microbiome. *eLife* **8**, e46540 (2019).
25. Dillard, K. E. et al. Mechanism of broad-spectrum Cas9 inhibition by AcrIIA11. Preprint at *bioRxiv* https://doi.org/10.1101/2021.09.15.460536 (2021).
26. Nishimasu, H. et al. Crystal structure of Cas9 in complex with guide RNA and target DNA. *Cell* **156**, 935–949 (2014).
27. Nishimasu, H. et al. Crystal structure of *Staphylococcus aureus* Cas9. *Cell* **162**, 1113–1126 (2015).
28. Swarts, D. C. & Jinek, M. Mechanistic insights into the *cis*- and *trans*-acting DNase activities of Cas12a. *Mol. Cell* **73**, 589–600 (2019).
29. Swarts, D. C., van der Oost, J. & Jinek, M. Structural basis for guide RNA processing and seed-dependent DNA targeting by CRISPR–Cas12a. *Mol. Cell* **66**, 221–233 (2017).
30. Chen, J. S. et al. CRISPR–Cas12a target binding unleashes indiscriminate single-stranded DNase activity. *Science* **360**, 436–439 (2018).
31. Watters, K. E., Fellmann, C., Bai, H. B., Ren, S. M. & Doudna, J. A. Systematic discovery of natural CRISPR–Cas12a inhibitors. *Science* **362**, 236–239 (2018).
32. Zhang, J. H., Chung, T. D. & Oldenburg, K. R. A simple statistical parameter for use in evaluation and validation of high throughput screening assays. *J. Biomol. Screen.* **4**, 67–73 (1999).
33. Fu, Y. et al. High-frequency off-target mutagenesis induced by CRISPR–Cas nucleases in human cells. *Nat. Biotechnol.* **31**, 822–826 (2013).
34. Lim, D. et al. Engineering designer beta cells with a CRISPR–Cas9 conjugation platform. *Nat. Commun.* **11**, 4043 (2020).
35. Flaxman, H. A., Chang, C. F., Wu, H. Y., Nakamoto, C. H. & Woo, C. M. A binding site hotspot map of the FKBP12–rapamycin–FRB ternary complex by photoaffinity labeling and mass spectrometry-based proteomics. *J. Am. Chem. Soc.* **141**, 11759–11764 (2019).
36. Miyamoto, D. K., Flaxman, H. A., Wu, H. Y., Gao, J. & Woo, C. M. Discovery of a celecoxib binding site on prostaglandin E synthase (PTGES) with a cleavable chelation-assisted biotin probe. *ACS Chem. Biol.* **14**, 2527–2532 (2019).
37. Joiner, C. M., Levine, Z. G., Aonbangkhen, C., Woo, C. M. & Walker, S. Aspartate residues far from the active site drive O-GlcNAc transferase substrate selection. *J. Am. Chem. Soc.* **141**, 12974–12978 (2019).
38. Jiang, F. et al. Structures of a CRISPR–Cas9 R-loop complex primed for DNA cleavage. *Science* **351**, 867–871 (2016).
39. Seelig, G., Soloveichik, D., Zhang, D. Y. & Winfree, E. Enzyme-free nucleic acid logic circuits. *Science* **314**, 1585–1588 (2006).
40. Qian, L. & Winfree, E. Scaling up digital circuit computation with DNA strand displacement cascades. *Science* **332**, 1196–1201 (2011).
41. Bondeson, D. P. et al. Lessons in PROTAC design from selective degradation with a promiscuous warhead. *Cell Chem. Biol.* **25**, 78–87 (2018).
42. Lai, A. C. & Crews, C. M. Induced protein degradation: an emerging drug discovery paradigm. *Nat. Rev. Drug Discov.* **16**, 101–114 (2017).

Methods

In vitro transcription of gRNA

Linear DNA fragments containing the T7 promoter sequence upstream of the desired gRNA protospacer and the gRNA backbone were generated by PCR (Q5 Hot Start MasterMix, New England Biolabs) using the primers listed in Supplementary Table 4. The fragments were concentrated on MinElute columns (Qiagen). The gRNA was transcribed using a HiScribe T7 high yield RNA synthesis kit (New England Biolabs) at 37 °C for 14–16 h with 400 ng of linear template per 30 µl of reaction. The gRNA was purified using a MEGAClear transcription clean-up kit (ThermoFisher) according to the manufacturer's instructions. Purified gRNAs were stored in aliquots at −80 °C.

Generation of CAA substrates

Oligonucleotide-annealing solutions were prepared by mixing complementary strands (10 µM final concentration) together in 1×Cas9 assay buffer (20 mM Tris–HCl, pH 7.5, 100 mM KCl and 5 mM $MgCl_2$). The oligonucleotides were annealed by heating to 95 °C for 5 min, followed by slow cooling to 25 °C at a rate of 0.1 °C s^{-1} to produce a double-stranded oligonucleotide. Complementary strands were purchased from Integrated DNA Technologies.

Fluorescence polarization assay for optimization of substrates of SaCas9 and FnCas12a

The fluorescence polarization assay for SaCas9 and FnCas12a (Extended Data Fig. 1b–d) was performed using a previously reported method with the substrates mentioned in Supplementary Table 2 (ref. [17]).

Optimization of the CAA

First, we optimized various components and conditions of the CAA for Cas enzyme activity and generality with different Cas enzymes, such as SpCas9 (Fig. 1b), SaCas9 (Extended Data Fig. 1f) and FnCas12a (Extended Data Fig. 2a,b). Typically, SpCas9:gRNA (1:1.2) RNP was pre-formed at 1 µM in Cas9 assay buffer for 5 min at 4 °C before dilution to 10 nM in Cas9 assay buffer (2× final concentration). The 2×Cas9 stock (25 µl aliquots) was manually dispensed to a black 384-well plate (Corning, 3575) using an electronic pipette. Apo SpCas9 (without gRNA) was used at the same concentration as a control for no activity (mock inhibition). Following this pre-annealed Alexa Fluor 647-labelled substrate and quencher were also diluted to 1 nM and 5 nM, respectively, in Cas9 assay buffer (2×stock solution). Next, 25 µl of the substrate/quencher solution was added manually to each well of the Cas9-containing 384-well plates using an electronic pipette and incubated at 37 °C for 2.5 h. The fluorescence signals were read with the microplate reader set to read Alexa Fluor 647 fluorescence. The assay was performed similarly with SaCas9 and FnCas12a using the respective enzyme, gRNA, and substrate and quencher oligonucleotides. We similarly divulged the effect of PAM sequences of dsDNA on its assay specificity using TGG, TGC and AAC PAM-containing substrates for SpCas9 (Fig. 1c); ACGGGT, ACGGTT and TGCCCA PAM substrate for SaCas9 (Fig. 1f); and TTTC, TTGC, AAAG PAM substrates for FnCpf1 (Fig. 2b,c). We also optimized the effective concentration of dsAF647 and ssAF647 fluorophores (Fig. 3a), double-stranded substrate-to-SpCas9 RNP ratio (Fig. 3b) and substrate-to-quencher ratio (Fig. 3c) on assay performance. Similarly, we performed a time-course experiment to establish the time required for maximum completion of the reaction at various substrate-to-SpCas9 RNP ratios (Fig. 3d).

Validation of the CAA

We further validated the CAA using protein inhibitors, such as AcrIIA4 (Fig. 1e), AcrIIA11 (Extended Data Fig. 1e) and AcrVA1 (Fig. 2e), that inhibit Cas enzymes through different mechanisms. Typically, active SpCas9:gRNA (1:1.2) RNP was pre-formed at 1 µM in Cas9 assay buffer for 5 min at 4 °C before dilution to 50 nM in Cas9 assay buffer (10× final concentration). The 2×Cas9 stock (25 µl) was manually dispensed to a black 384-well plate (Corning, 3575) using an electronic pipette. Apo SpCas9 was used at the same concentration as a control for no activity. Various concentrations (final concentration of 0–10 µM) of 10× AcrIIA4 or AcrIIA11 were manually added using an electronic pipette and incubated with SpCas9 for at least 30 min at room temperature. Following this, pre-annealed Alexa Fluor 647-labelled substrate and quencher were also diluted to 10 nM and 50 nM, respectively, in Cas9 assay buffer (10×stock solution). Next, 25 µl of the substrate/quencher solution was added manually to each well of the Cas9-containing 384-well plates using an electronic pipette and incubated at 37 °C for 2.5 h. The fluorescence signals were read with the microplate reader set to read Alexa Fluor 647 fluorescence. Similarly, CAA for FnCas12a was validated using its protein inhibitor AcrVA1.

CAA

High-throughput screening with the CAA was performed as follows. Active SpCas9:gRNA (1:1.2) RNP was pre-formed at 1 µM in Cas9 assay buffer for 5 min at 4 °C before dilution to 10 nM in Cas9 assay buffer (2× final concentration). Using a liquid handling dispenser, 25 µl of the 2×Cas9 stock was dispensed to a black 384-well plate (Corning, 3575). Apo SpCas9 was used at the same concentration as a control for no activity. Compound libraries and DMSO controls were added via pin transfer of 100 nl from 10 mM or 5 mg ml^{-1} stocks in DMSO and incubated with SpCas9 for at least 30 min at room temperature. Compound autofluorescence was measured at this time using a microplate reader (Envision operated by Envision Manager 1.13, PerkinElmer) set to read Alexa Fluor 647 fluorescence. Pre-annealed Alexa Fluor 647-labelled substrate and quencher were then also diluted to 1 nM and 5 nM, respectively, in Cas9 assay buffer (2×stock solution). Next, 25 µl of the substrate/quencher solution was added to each well of the Cas9-containing 384-well plates using a liquid handling dispenser and incubated at 37 °C for 2.5 h. The fluorescence signals from Alexa Fluor 647 were read with the microplate reader. Compounds were screened in duplicate. Data were processed to calculate the Z-score $((x-\mu)/\sigma)$ values, where x is the signal from the sample, and μ and σ are the average and s.d., respectively, from the negative controls. Potential hit compounds (Z score > 3) were prioritized for further screening. Some compounds exhibited normalized inhibition of less than zero (Fig. 3f), which arises from the quenching of the Alexa Fluor 647 fluorescence, as measured from the abovementioned counter screening. Those compounds were excluded from further testing. The detailed protocol for can be found at *Protocol Exchange*[43].

Gel-monitored cleavage assays with FAM oligonucleotides

For SpCas9, RNP complex was formed by mixing SpCas9 and Spinach-targeting gRNA at room temperature for 15 min at a 1:1.2 ratio. Next, FAM-labelled dsDNA substrates were added to the mixture to a final concentration of 20 nM FAM-dsDNA with 100 nM SpCas9 and 120 nM gRNA in 30 µl. The mixture was incubated at 37 °C for 3 h, resolved on a 4–20% acrylamide gel and imaged on an Azure 600 system (Azure Biosystem) under the blue fluorescence channel. The same reaction conditions were used for SaCas9. For AsCas12, LbCas12a and FnCas12a, 100 nM FAM-dsDNA, 500 nM nuclease and 600 nM gRNA were used. Native acrylamide gel electrophoresis (Fig. 1d) or urea-based denaturing gel electrophoresis (Figs. 1g, 2d and Extended Data Fig. 2c) were performed for resolving the reaction mixtures.

Cell culture

U2OS.eGFP.PEST cells (gift from J. K. Joung's laboratory) and HEK293T cells (American Type Culture Collection, CRL-3216) were maintained in Dulbecco's modified eagle medium supplemented with 10% fetal bovine serum, 1×penicillin–streptomycin and 1 mM pyruvate. The cells were routinely tested for mycoplasma contamination using a Universal mycoplasma detection kit (American Type Culture Collection, 30-1012K). None of the cell lines were authenticated.

eGFP-disruption assay

For the SAR and dose-response studies, 300,000 U2OS.eGFP.PEST cells were nucleofected with 300 ng SpCas9 plasmid (Addgene, 43861) and 30 ng *eGFP*-targeting gRNA plasmid (Addgene, 47511)[33] using an SE cell line 4D-Nucleofector X kit (Lonza) following the pulse program DN-100. For RNP-based genome editing, 10 pmol SpCas9 (GenScript, Z03385) and 12 pmol gRNA were mixed and incubated for 5 min. For RNP-based genome editing with LbCas12a, 15 pmol LbCas12a (New England Biolabs, M0653T) and 20 pmol *crispr* RNA (spacer: 5′-CGTCGCCGTCCAGCTCGACC-3′) were used due to its lower basal activity. Cells were nucleofected with the resulting RNP complex using the same pulse program. The cells were transferred to a 96-well plate at a density of 25,000 cells per well and incubated with the indicated amount of compound for 24 h. The cells were then fixed with 4% paraformaldehyde solution in PBS and nuclei were stained using HCS NuclearMask blue stain (Invitrogen). Imaging was performed using an ImageXpress micro high-content analysis system (Molecular Devices) or an Operetta CLS high-content analysis system (PerkinElmer). Data analysis was performed using MetaXpress (Molecular Devices) or Operetta Harmony 4.8 (PerkinElmer). For the secondary screening assay, compounds were first dispensed to a 384-well plate using a Hewlett Packard D300e and resuspended in 25 µl medium. Nucleofected cells (5,000) were then added to each well (in duplicate) to yield a final compound concentration of 20 µM. The cells were incubated for 24 h and imaging was performed. Transfection with SpCas9 plasmid only served as a positive control representing 100% inhibition, and transfection with SpCas9 and gRNA plasmids and treatment with DMSO served as a negative control. The *Z* scores were calculated for each compound and compounds with a *Z* score of >2 were selected and validated in additional orthogonal cellular assays.

HiBiT-knock-in assay

Approximately 400,000 HEK293T cells were nucleofected with 400 ng SpCas9 plasmid, 40 ng *GAPDH*-targeting gRNA plasmid and 40 pmol single-stranded oligodeoxynucleotide using a SF cell line 4D-Nucleofector X kit (Lonza) following the pulse program DS-150. For RNP-based genome editing, 10 pmol Cas9 and 12 pmol gRNA were mixed and incubated for 5 min. Next, 20 pmol single-stranded oligodeoxynucleotide was added. The cells were nucleofected with the resulting mixture using the same pulse program. The cells were then transferred to a 96-well plate at a density of 35,000 cells per well and incubated with the indicated amount of compounds for 24 h. Cell viability was measured using PrestoBlue reagent (Thermo) with a SpectraMax M5 reader operated by SoftMax Pro 7.0 (Molecular Devices) at excitation and emission wavelengths of 544 and 590 nm, respectively. Luminescence measurements were then performed using a Nano-Glo HiBiT lytic detection system (Promega) according to the manufacturer's protocol with an EnVision multilabel plate reader (PerkinElmer) at an integration time of 0.5 s per well. The resulting luminescence signals were normalized based on the cell viability[34].

Compound–SpCas9 interaction in BLI

The experiments were performed in a 96-well format with a 180-µl reaction volume using biotin-BRD7586 and streptavidin sensors. To start, 1 µM of the biotinylated compound was loaded onto the sensors for 180 s in 20 mM Tris buffer (100 mM KCl, 5 mM $MgCl_2$, 1 mM DTT and 0.01% Tween, pH 7.4). The compound-loaded sensors were then allowed to associate with different concentrations of the SpCas9:gRNA complex (0.015–1 µM) for 300 s, followed by dissociation in reaction buffer. The reference sensor was loaded with compound and allowed to associate and dissociate in reaction buffer alone. Response curves were fitted with a 2:1 stoichiometric model and a global-fit steady-state analysis was performed using the manufacturer's protocol. The experiments were performed in triplicate. Control experiments were performed using a biotin-PEG3-azide. In this experiment, streptavidin sensors were associated with 1 µM biotin-PEG3-azide, 1 µM biotin-BRD7586 or reaction buffer alone. The sensors were then allowed to associate with different concentrations of SpCas9:gRNA complex (0.015–1 µM) or buffer alone.

STD NMR binding assay

All samples were prepared with 20 µM BRD7586 in a 20 mM Tris-d11 buffer (pH 7.4) in D_2O with or without 5 µM SpCas9:gRNA in a 3-mm NMR tube. Experiments were performed on a 600 MHz (^{19}F: 564.71 MHz) Bruker AVANCE III NMR spectrometer equipped with a 5-mm QCI-F CryoProbe and a SampleJet for automated sample handling. To acquire the spectra, a standard one-pulse STD experiment with WALTZ-16 for proton decoupling during acquisition, a recycle delay of 5 s and 256 scans were used. All spectra were recorded at 280 K. The NMR data were apodized with a 1-Hz exponential function before Fourier transformation. All spectra were baseline corrected, and peak widths and intensities were extracted using the automated line-fitting feature provided with the MNova software package.

Cell viability assay

HEK293T or U2OS.eGFP.PEST cells were plated in a 96-well plate at a density of 30,000 or 20,000 cells per well, respectively. The following day, the cells were treated with the indicated amount of compounds for 24 h. Cellular ATP levels were then measured using a CellTiter-Glo luminescent cell viability assay (Promega) with an EnVision multilabel plate reader (PerkinElmer) and an integration time of 0.5 s per well.

Targeted deep sequencing to detect indels at endogenous loci

U2OS.eGFP.PEST cells were nucleofected as described earlier for the *eGFP*-disruption assay, plated in a 24-well plate at a density of 150,000 cells per well and incubated with BRD7586 for 24 h. Next, the genomic DNA was extracted using a DNeasy blood and tissue kit (Qiagen). HEK293T cells were plated in a 24-well plate at a density of 100,000 cells per well. The cells were transfected with 500 ng SpCas9 plasmid and 250 ng of *EMX1*-, *VEGFA*- or *FANCF*-targeting gRNA plasmid using Lipofectamine 3000 (Invitrogen) the following day. The indicated amount of compound was added at the time of transfection, the cells were incubated for 24 or 48 h and genomic DNA was extracted. Next-generation-sequencing samples were prepared using a two-step PCR protocol. The next-generation-sequencing libraries were quantified using a KAPA library quantification kit (Roche) and diluted to 4 nM. Sequencing of the pooled library was performed using MiSeq reagent kit v2 and a MiSeq System operated by the MiSeq Control Software (Illumina). The percentage of indels in the demultiplexed sequence files was analysed using the CRISPResso2 software from the Pinello laboratory[44].

Immunoblotting

Approximately 500,000 U2OS.eGFP.PEST cells were nucleofected with 500 ng of SpCas9 plasmid as described earlier. The cells were then plated in a 12-well plate with the indicated amount of compound and incubated for 24 h. HEK293T cells were transfected with 500 ng SpCas9 plasmid as described earlier and incubated with the compound in a 24-well plate for 24 h. The cells were harvested and lysed using RIPA buffer containing Protease inhibitor cocktail (Roche). The lysate was cleared by centrifugation at 20,000*g* in 4 °C and the supernatant was taken to measure the protein concentration using a BCA assay. Approximately 10–20 µg of the total protein was used for immunoblotting. Rabbit anti-SpCas9 (Abcam, 89380; 1:1,000 dilution) and mouse anti-α-tubulin (CST, 3873; 1:2,000 dilution) were used as primary antibodies. IRDye 680RD donkey anti-rabbit IgG (LI-COR, 925-68073; 1:10,000 dilution) and IRDye 800CW donkey anti-mouse IgG (LI-COR, 925-32212; 1:10,000 dilution) were used as secondary antibodies. The fluorescence signals were detected using LI-COR Odyssey operated by LI-COR Image Studio.

Plasma stability assay

The stability of the compound in mouse plasma was assessed following a reported protocol[45]. BRD7586 (2 µM) was incubated with 50% mouse

plasma (K2 EDTA, BioIVT) in PBS for 2 h in duplicate. Propantheline was included as a control.

In vitro DNA cleavage assay

Inhibition of SpCas9 nuclease activity was assessed in an in vitro DNA cleavage assay 50-µl reaction volume in PBS buffer with 10 mM $MgCl_2 \cdot 6H_2O$. First, Cas9:gRNA complex (30 nM Cas9 (New England Biolabs) and 36 nM *eGFP*-targeting gRNA) was formed by mixing each component at a 1:1.2 (Cas9:gRNA) molar ratio with incubation at room temperature for 10 min. BRD7586 at doses of 0, 5, 10, 20, 30 and 40 µM were incubated with the Cas9:gRNA complex at 37 °C and 700 r.p.m. for 30 min. PCR-amplified target *eGFP* DNA (2 nM) was added after 30 min of compound incubation and the mixture was incubated at 37 °C and 700 r.p.m. for 30 min. Proteinase K (5 µl) was added and the samples were incubated at 37 °C and 700 r.p.m for 30 min to digest the Cas9. The resulting mixtures were purified using a MinElute PCR purification kit (Qiagen) and the eluted DNA was quantified using the Qubit HS DNA quantification method. Equal amounts of DNA samples were run on a 1% agarose E-gel (Invitrogen) for 7 min. Images were obtained using an Azure 600 system (Azure Biosystem) and quantification of band intensities was performed using ImageJ 1.52a.

Photo-crosslinking

Cas9 RNP complex was formed by mixing Cas9 (1 µM) and the *eGFP*-targeting gRNA (1 µM) in a binding buffer (HEPES 20 mM and KCl 100 mM, pH 7.6) for 15 min. Next, BRD7586 (5 µM) was added to the mixture when competition was required (the last lane of Fig. 7b). Finally, diazirine-BRD7586 was added (1 µM) and the mixture was incubated in a final reaction volume of 20 µl in a PCR tube for 20 min at room temperature. The mixture was irradiated with UV (365 nm) for 5 min on ice and then 2.5 µl of 10% RapiGest SF solution in PBS was added. Click chemistry was initiated by adding 100 µM TAMRA-azide (Sigma, 760757), 350 µM Cu-TBTA and 1.5 mM ascorbate in a final reaction volume of 27 µl. The reaction was conducted for 1 h at 30 °C, followed immediately by SDS–PAGE. The fluorescence gel scanning was conducted using an Azure 600 system (Azure Biosystem) to detect the TAMRA fluorescence.

Validation of target engagement in live cells

HEK293T cells were plated in a six-well plate (400,000 cells per well). The following day, the cells were transfected with 2 µg Cas9 expression plasmid (pX330; Addgene, 42230)[46] using Lipofectamine 3000 (Invitrogen). Eight hours after transfection, the cells were split into four wells of a 12-well plate. After transfection for 24 h, the cells were treated with DMSO, diazirine-BRD7586 (20 µM) or diazirine-BRD7586 with BRD7586 (both at 20 µM) for 2 h. The cells were washed once with PBS and 500 µl fresh PBS was added to each well. The plate was placed on ice and the cells were irradiated with UV (365 nm) for 15 min. After the removal of PBS, the cells were stored at −80 °C until further analysis. Thawed cells were resuspended in a lysis buffer (25 mM HEPES, 50 mM KCl, 1% Triton X-100 and 1×protease inhibitor cocktail, pH 7.4; 200 µl per well) and a brief sonication was performed to ensure cell lysis. Next, click chemistry was performed with 100 µM biotin-azide, 350 µM Cu-TBTA and 1.5 mM ascorbate. The reaction was allowed to proceed for 2 h at room temperature with mild rotation, after which the proteins were precipitated by the addition of cold methanol (fivefold volume of the reaction mixture) to the mixture and refrigeration at −80 °C for >2 h. A protein pellet was obtained by centrifugation for 10 min at 16,000*g* and 4 °C. The pellet was washed with cold PBS:methanol (1:5 vol/vol), air-dried for 10 min and resuspended in 100 µl of 1.2% SDS solution in PBS. Heating at 37 °C was required for complete solubilization of the pellet. An aliquot of the solution (10 µl) was reserved for future analysis as an input. The remaining 90 µl were diluted with PBS and incubated with 40 µl of Streptavidin magnetic beads (Thermo, 88816) in a final volume of 720 µl. The mixture was incubated for several hours at room temperature with mild rotation. The beads were then washed four times with 0.2% SDS solution in PBS (600 µl each). Finally, the proteins were eluted from the beads by heating in an SDS–PAGE buffer. Immunoblotting was performed using mouse anti-SpCas9 (Abcam, 191468; 1:1,000 dilution) and anti-mouse HRP (CST, 7076; 1:5,000 dilution).

Protein purification, binding-site identification and chemical synthesis

The methods used for the purification of Cas nucleases, identification of BRD7586-binding sites and chemical synthesis are described in the Supplementary Information.

Statistics and reproducibility

Two-tailed and unpaired *t*-tests were performed using Microsoft Excel 2016 to compare the means of two samples and *P* values from the tests are presented in the figure legends. Data were analysed and plotted using Prism 8 (GraphPad). Independent experiments reported here were performed by different researchers using independently prepared biochemical reagents, or independent splits of the mammalian cell types were used. Representative images from two independent replicates are shown in Figs. 1d and 7b,c. Images from a single experiment are shown for Figs. 1g, 2d and Extended Data Fig. 2c. Representative images from six independent replicates are shown for Fig. 4b. Representative images from two (HEK293T) or three (U2OS.eGFP.PEST) independent replicates are shown for Fig. 4g. Images from four independent replicates are shown for Extended Data Fig. 3c. Representative images from two independent experiments are shown for Extended Data Figs. 4a,b and 7a.

Reporting summary

Further information on research design is available in the Nature Research Reporting Summary linked to this article.

Data availability

Data generated in this study are provided in the manuscript, Supplementary Information and Source Data. Plasmids from Addgene (plasmids 43861, https://www.addgene.org/43861; 47511, https://www.addgene.org/47511; and 42230, https://www.addgene.org/42230) were used in this study. Structural information from Protein Data Bank (ID: 5F9R) was used in this study. High-throughput sequencing data have been deposited at the NCBI Sequence Read Archive database under accession number PRJNA862731. Source data are provided with this paper. All other data supporting the findings of this study are available from the corresponding author on reasonable request.

Code availability

No code or algorithm was generated in this study.

References

43. Lim, D., Sreekanth, V. & Choudhary, A. Identifying anti-CRISPR small molecules via high-throughput assay. *Protoc. Exch.* (2022).
44. Clement, K. et al. CRISPResso2 provides accurate and rapid genome editing sequence analysis. *Nat. Biotech.* **37**, 224–226 (2019).
45. Di, L., Kerns, E. H., Hong, Y. & Chen, H. Development and application of high throughput plasma stability assay for drug discovery. *Int. J. Pharm.* **297**, 110–119 (2005).
46. Cong, L. et al. Multiplex genome engineering using CRISPR/Cas systems. *Science* **339**, 819–823 (2013).

Acknowledgements

This work was supported by the Burroughs Wellcome Fund (Career Award at the Scientific Interface to A.C.), DARPA (N66001-17-2-4055 to A.C.) and NIH (R01GM132825 and R01GM137606 to A.C.). We thank J. K. Joung for providing U2OS.eGFP.PEST cells and H. S. Malik for providing AcrIIA11 protein expression plasmid.

Author contributions

D.L., Q.Z., K.J.C., B.K.L., M.L., P.K., V.S. and A.C. planned the research. D.L., Q.Z., K.J.C., B.K.L., M.L., P.K., V.S., Y.A., C.M.W. and A.C. designed the experiments. D.L., Q.Z., K.J.C., B.K.L., M.L., P.K., V.S., R.P., S.K.C., S.A.G., B.M., S.L., Y.A. and M.F.M. performed the experiments. D.L., Q.Z., K.J.C., B.K.L., M.L., P.K., V.S., R.P., S.K.C., S.A.G., B.M., S.L., Y.A., D.B.T., H.K.K.S., M.F,M., V.D., P.A.C., B.K.W., C.M.W, G.M.C. and A.C. analysed the data. D.L., Q.Z., K.J.C., B.K.L., M.L., P.K., V.S. and A.C. wrote the manuscript. A.C. supervised the research. R.P. and S.K.C. contributed equally to this work.

Competing interests

Broad Institute has filed a patent application including work described herein (US Provisional Patent Application Number 63/393,788; inventors: A.C., D.L., Q.Z., K.J.C., B.K.L., M.L., P.K. and V.S.). The remaining authors declare no competing interests.

Additional information

Extended data is available for this paper at https://doi.org/10.1038/s41556-022-01005-8.

Supplementary information The online version contains supplementary material available at https://doi.org/10.1038/s41556-022-01005-8.

Correspondence and requests for materials should be addressed to Amit Choudhary.

Peer review information *Nature Cell Biology* thanks Keith T. Gagnon and the other, anonymous, reviewer(s) for their contribution to the peer review of this work.

Reprints and permissions information is available at www.nature.com/reprints.

https://doi.org/10.1038/s41556-022-01005-8

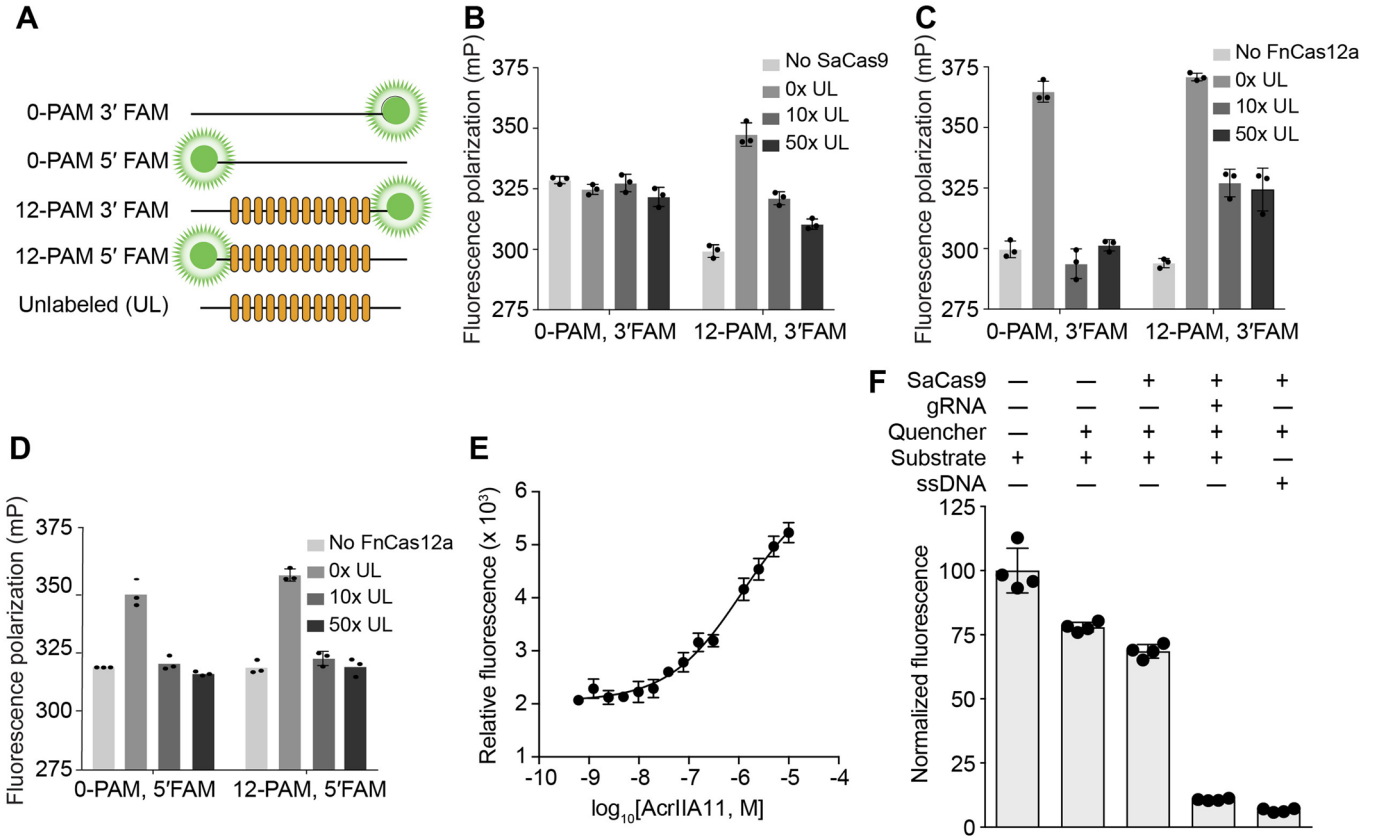

Extended Data Fig. 1 | Validation of the CAA. (a) Schematic of the differently labelled PAM fluorescence polarization substrates. **(b)** Fluorescence polarization assay comparing 0-PAM and 12-PAM substrates with SaCas9 at multiple concentrations of unlabelled ligand. Substrates were labelled with FAM on the 3′ end. SaCas9 showed specificity for the 12-PAM substrate that decreased with increasing amounts of unlabelled competitor. Error bars represent mean ± SD from 3 independent replicates. For '0x UL' compared to 'No SaCas9', $p = 0.061$ with the 0-PAM DNA and $p = 1.1 \times 10^{-4}$ with the 12-PAM DNA (unpaired t-test, two-tailed). **(c)** Fluorescence polarization assay comparing 0-PAM and 12-PAM substrates with FnCas12a at multiple concentrations of unlabelled ligand. Substrates were labelled with FAM on the 3′ end. FnCas12a showed no specificity dependent upon the presence of PAM-binding sites. Error bars represent mean ± SD from 3 independent replicates. For '0x UL' compared to 'No FnCas12a', $p = 3.5 \times 10^{-5}$ with the 0-PAM and $p = 7.4 \times 10^{-7}$ with the 12-PAM DNA (unpaired t-test, two-tailed). **(d)** Fluorescence polarization assay comparing 0-PAM and 12-PAM substrates with FnCas12a at multiple concentrations of unlabelled ligand. Substrates were labelled with FAM on the 5′ end. FnCas12a showed no specificity dependent upon the presence of PAM-binding sites. Error bars represent mean ± SD from 3 independent replicates. For '0x UL' compared to 'No FnCas12a', $p = 6.2 \times 10^{-4}$ with the 0-PAM and $p = 6.2 \times 10^{-5}$ with the 12-PAM DNA (unpaired t-test, two-tailed). **(e)** Inhibition of SpCas9 by AcrIIA11 monitored by the CAA. Error bars represent mean ± SD from 4 independent replicates. For 10 μM AcrIIA11 compared to buffer only, $p = 1.6 \times 10^{-7}$ (unpaired t-test, two-tailed). **(f)** The fluorescence of the SaCas9-specific substrate is not quenched in the presence of quencher unless the duplex is disrupted by cleavage via an active SaCas9:gRNA complex. A single DNA strand containing the fluorophore (SS-DNA) can be completely quenched in the absence of an unlabelled complementary strand. Error bars represent mean ± SD from 4 independent replicates. For SaCas9:gRNA (4th bar) compared to SaCas9 only (3rd bar). $p = 1.1 \times 10^{-8}$ (unpaired t-test, two-tailed).

https://doi.org/10.1038/s41556-022-01005-8

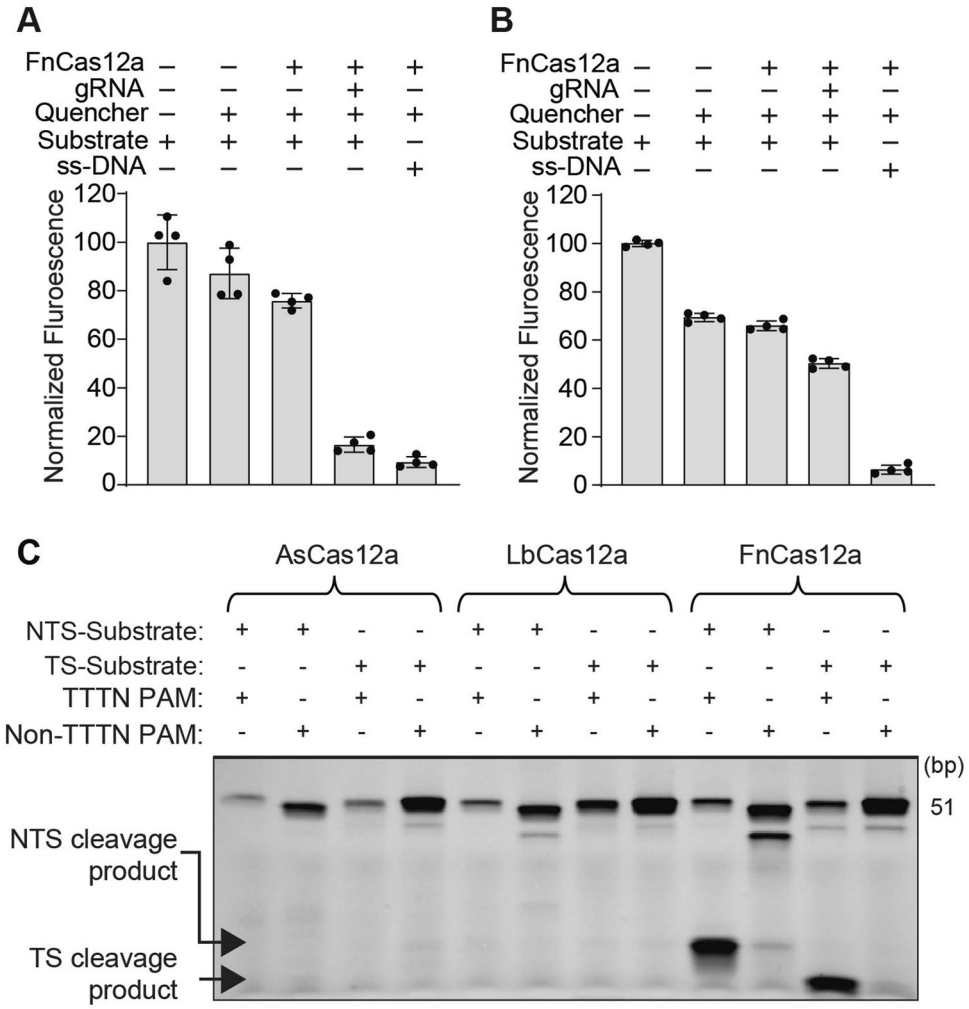

Extended Data Fig. 2 | Generalization of the CAA. (a) Demonstration of FnCas12a CAA. The fluorescence of the FnCas12a-specific substrate labelled on the non-targeting strand (NTS) is not quenched in the presence of quencher unless the duplex is disrupted by cleavage via an active FnCas12a:gRNA complex. A single DNA strand containing the fluorophore (SS-DNA) can be completely quenched in the absence of an unlabelled complementary strand. Error bars represent mean ± SD from 4 independent replicates. For FnCas12a:gRNA (4th bar) compared to FnCas12a only (3rd bar), $p = 1.5 \times 10^{-7}$ (unpaired t-test, two-tailed). **(b)** Demonstration of FnCas12a CAA. The fluorescence of the FnCas12a-specific substrate labelled on the targeting strand (TS) is quenched poorly even in the presence of active FnCas12a:gRNA complex. Error bars represent mean ± SD from 4 independent replicates. For FnCas12a:gRNA (4th bar) compared to FnCas12a only (3rd bar), $p = 3.3 \times 10^{-5}$ (unpaired t-test, two-tailed). **(c)** Gel-monitored cleavage of FAM-labelled oligos (20 nM) by AsCas12a (100 nM), LbCas12a (100 nM), and FnCas12a (100 nM) in a PAM-dependent manner.

https://doi.org/10.1038/s41556-022-01005-8

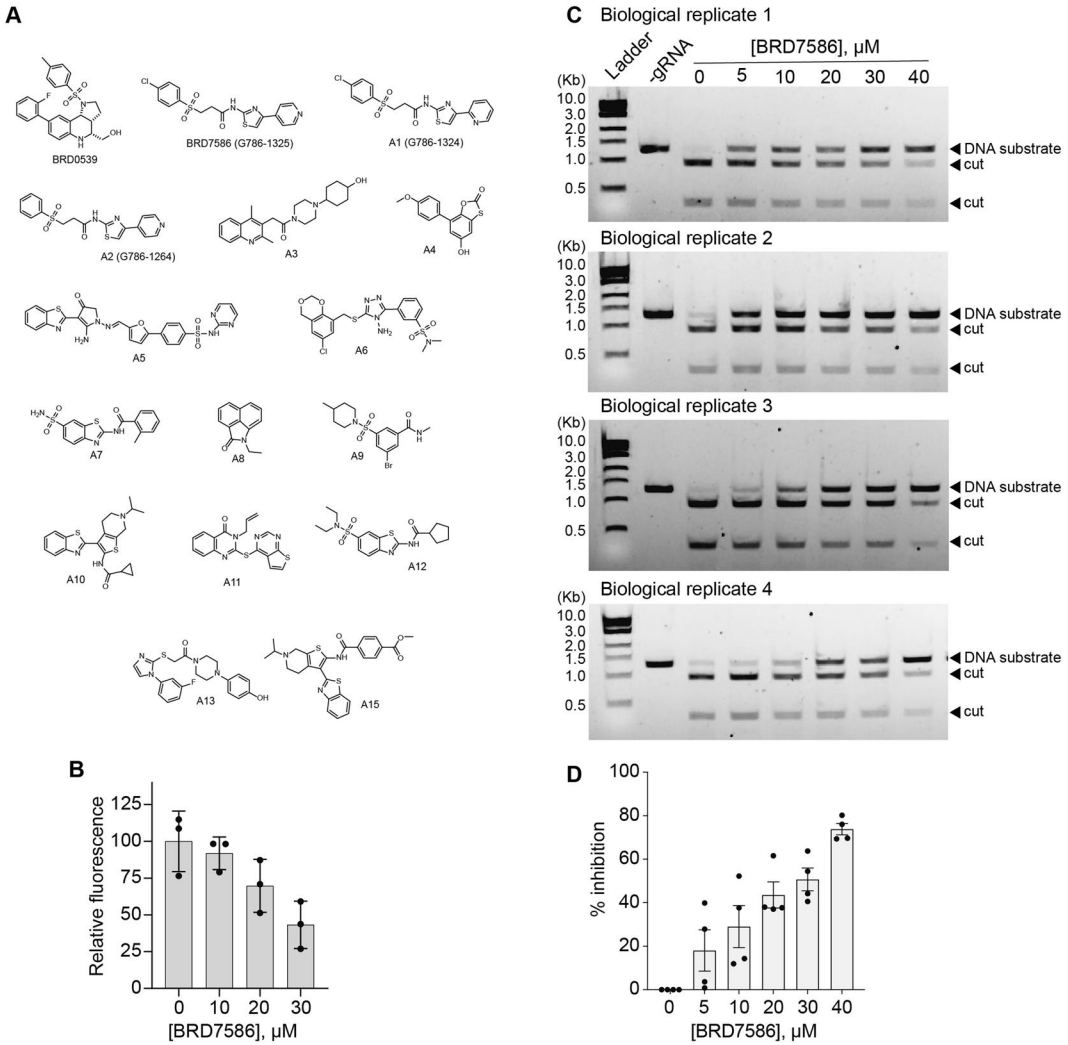

Extended Data Fig. 3 | Biochemical validation of BRD7586. (a) Hit compounds (Z score > 3σ) identified in both the primary screen and secondary screens. Compounds were compared to BRD0539, a compound previously identified as an SpCas9 DNA-binding inhibitor. **(b)** Dose-dependent inhibition of SpCas9 by BRD7586 in the CAA. Error bars represent mean ± SD from 3 independent replicates. For 30 µM of BRD7586 compared to DMSO, p = 0.020 (unpaired t-test, two-tailed). **(c)** Gel electrophoresis-based monitoring of dose-dependent inhibition of SpCas9 by BRD7586 from *in vitro* DNA cleavage assay. Images from 4 independent replicates are shown. **(d)** Quantification of the inhibition from the above *in vitro* DNA cleavage assay. Error bars represent mean ± SD from 4 biological replicates. For 40 µM (6th bar) compared to DMSO (1st bar), $p = 1.3 \times 10^{-7}$ (unpaired t-test, two-tailed).

https://doi.org/10.1038/s41556-022-01005-8

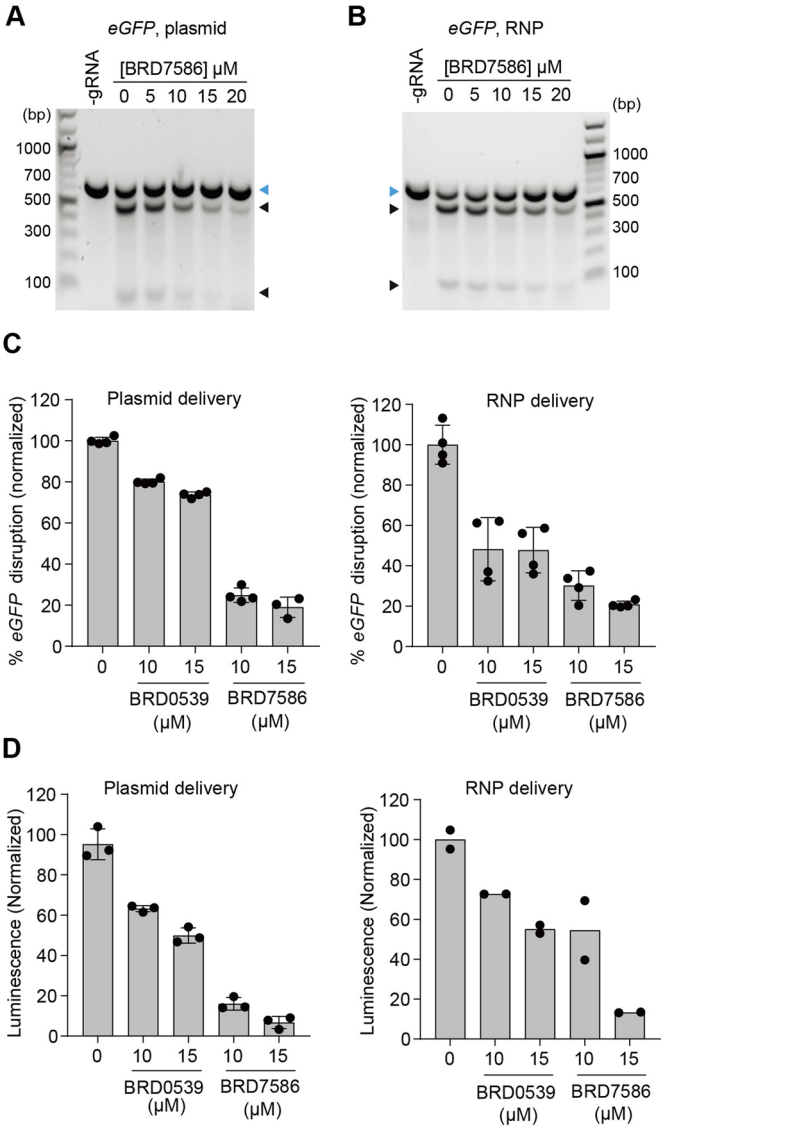

Extended Data Fig. 4 | Validation of BRD7586 in cells. (**a**, **b**) T7E1 assay for detecting indels at the *eGFP* gene. U2OS.eGFP.PEST cells were nucleofected with **(a)** plasmid or **(b)** RNP, and incubated with BRD7586 for 24 h. Blue arrowheads indicate uncleaved DNA and black arrowheads indicate cleaved DNA. (**c**) Inhibition of SpCas9 by BRD0539 and BRD7586 in the eGFP disruption assay using plasmid delivery method (left) and RNP delivery method (right) (U2OS.eGFP.PEST cells, 24 h). Error bars represent mean ± SD from 3 (5th bar in plasmid delivery) or 4 (1st to 4th bars in plasmid delivery and all bars in RNP delivery) independent replicates. For the plasmid-based assay, $p = 3.5 \times 10^{-7}$ for BRD0539 and $p = 1.2 \times 10^{-5}$ for BRD7586 at 15 μM compared to DMSO. For the RNP-based assay, $p = 4.1 \times 10^{-4}$ for BRD0539 and $p = 3.6 \times 10^{-6}$ for BRD7586 at 15 μM compared to DMSO (unpaired t-test, two-tailed). **(d)** Inhibition of SpCas9 by BRD0539 and BRD7568 in the *HiBiT* knock-in assay using plasmid delivery method (left) and RNP delivery method (right) in HEK293T cells (48 h). Error bars represent mean ± SD from 3 independent replicates for the plasmid delivery. Data represents mean from 2 independent replicates for the RNP delivery. For the plasmid delivery, $p = 7.8 \times 10^{-4}$ for BRD0539 at 15 μM compared to DMSO, and $p = 4.9 \times 10^{-5}$ for BRD7586 at 15 μM compared to DMSO (unpaired t-test, two-tailed).

https://doi.org/10.1038/s41556-022-01005-8

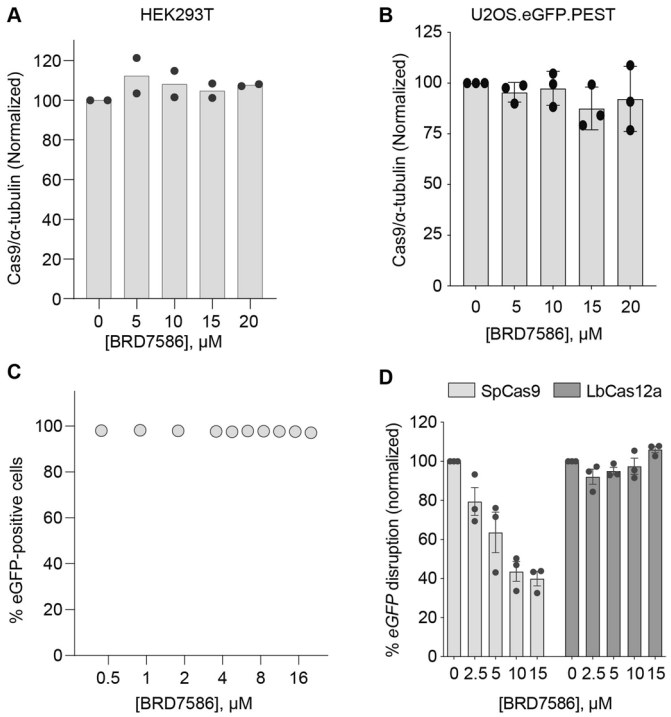

Extended Data Fig. 5 | Counter assays to validate BRD7586 in cells. (**a**, **b**) Immunoblotting analysis of SpCas9 expression in (**a**) HEK293T cells (data represent mean from 2 independent experiments) or (**b**) U2OS.eGFP.PEST cells (error bars represent mean ± SD from 3 independent experiments) transfected with SpCas9 plasmid and incubated with BRD7586 for 24 h. For BRD7586 at 20 μM compared to DMSO in U2OS.eGFP.PEST cells, p = 0.49 (unpaired t-test, two-tailed). (**c**) Changes in the fluorescence intensity from U2OS.eGFP.PEST cells in the presence of BRD7586. Cells were treated with the compound for 24 h, and the fluorescence intensity was measured to calculate the fraction of eGFP-positive populations. Means from 3 independent experiments are shown. Due to the low SD, error bars cannot be shown. For BRD7586 at 20 μM compared to DMSO, p = 0.14 (unpaired t-test, two-tailed). (**d**) Dose-dependent inhibition of SpCas9 or LbCas12a by BRD7586 in the eGFP disruption assay using RNP delivery methods (U2OS.eGFP.PEST cells, 24 h). Error bars represent mean ± SD from 3 independent experiments. For SpCas9, $p = 8.3 \times 10^{-5}$ with BRD7586 at 15 μM compared to DMSO. For LbCas12a, p = 0.023 with BRD7586 at 15 μM compared to DMSO (unpaired t-test, two-tailed).

https://doi.org/10.1038/s41556-022-01005-8

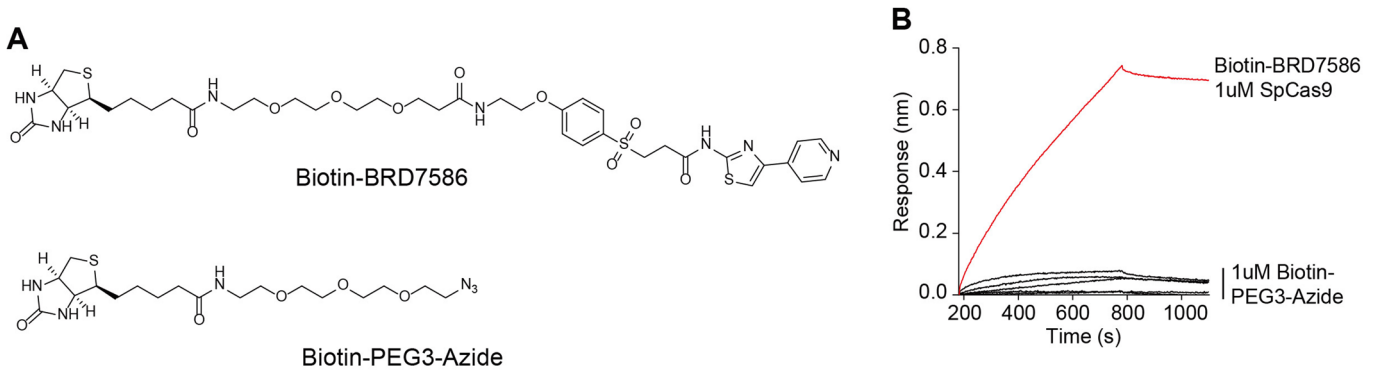

Extended Data Fig. 6 | Validation of the binding between BRD7586 and SpCas9. (**a**) Structure of Biotin-BRD7586 and Biotin-PEG3-Azide control. (**b**) Control BLI binding plot for Biotin-PEG3-azide and SpCas9:gRNA complex. BLI experiment was performed using 1 μM of Biotin-PEG3-azide on streptavidin sensors followed by association with different concentrations of SpCas9:gRNA complex and subsequent dissociation. BLI signal of biotin-BRD7586 and 1 μM SpCas9:gRNA complex is marked in red for comparison.

https://doi.org/10.1038/s41556-022-01005-8

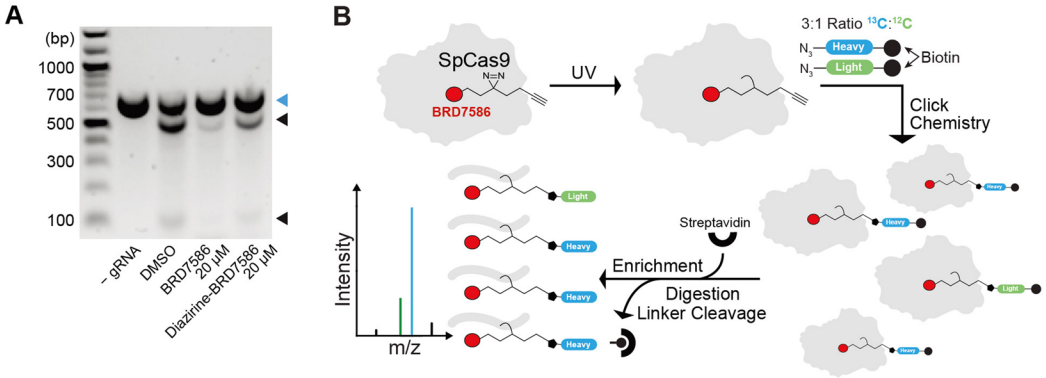

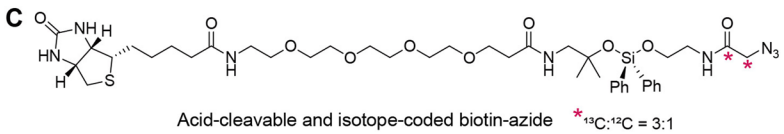

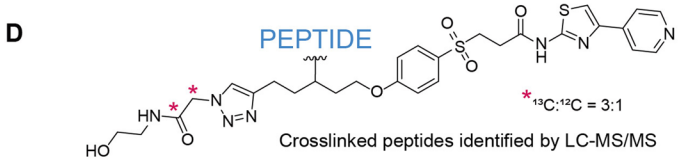

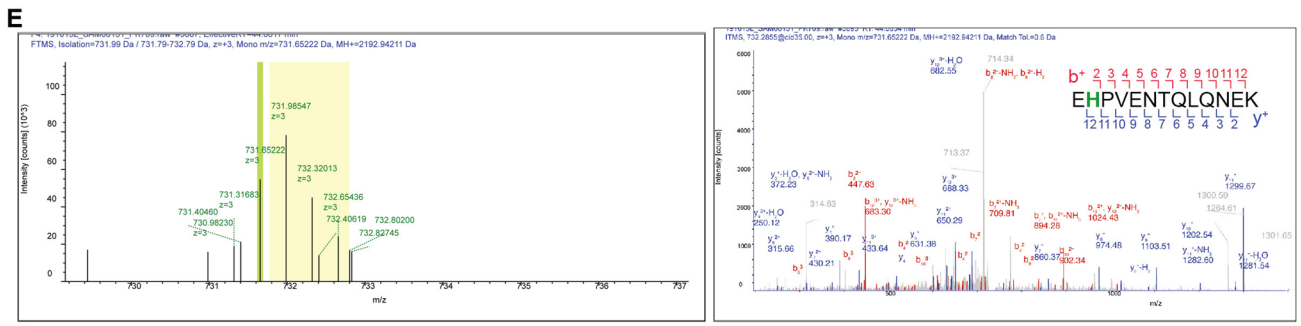

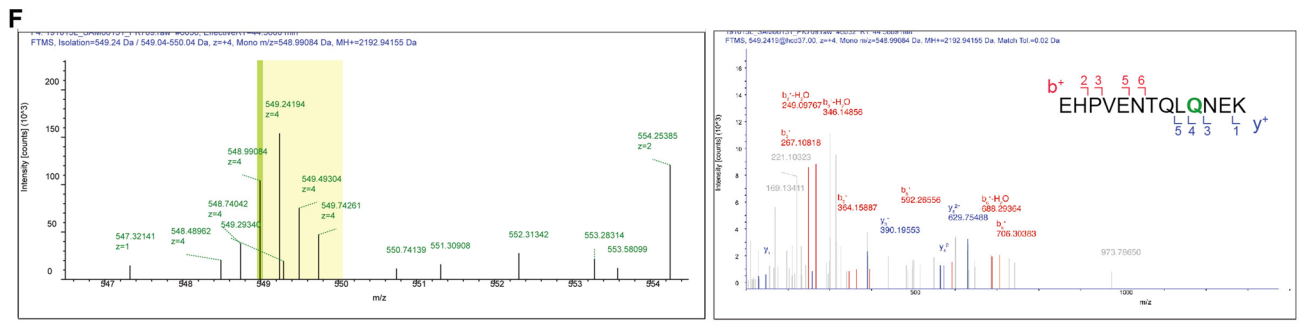

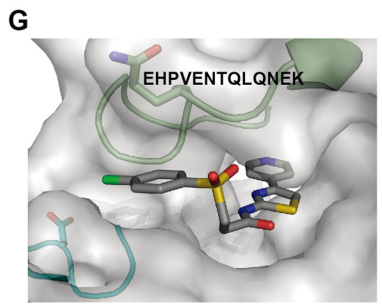

Extended Data Fig. 7 | See next page for caption.

https://doi.org/10.1038/s41556-022-01005-8

Extended Data Fig. 7 | Mechanism-of-action studies of BRD7586. (**a**) T7E1 assay for measuring the activity of Diazirine-BRD7586. U2OS.eGFP.PEST cells were nucleofected with Cas9 plasmid and eGFP-targeting plasmid, and the cells were incubated with the compounds for 24 h. Blue arrowheads indicate uncleaved DNA while black arrowheads indicate cleaved DNA from the T7E1 reaction. (**b**) Workflow of the chemoproteomics experiments using the diazirine-based photo-crosslinking probe to identify binding sites of BRD7586 on SpCas9. (**c**) Chemical structure of the acid-cleavable and isotope-coded biotin-azide used for chemoproteomics experiments. (**d**) Structure of the peptide-compound conjugates to be detected from the mass spectrometry. Note the 3:1 ratio of the isotope tag that allows reliable identification of the conjugates. (E-F) Examples of the mass spectra obtained from the chemoproteomics experiments. For the detailed information of identified peptides, see Supplementary Table 8. The isotope patterns are shown in MS1 spectra. The probe-conjugated residues are shown as green labels in MS2 spectra. (**g**) Proposed binding pocket of BRD7586 on SpCas9. BRD7586 was docked to SpCas9 at the HNH-nuclease and helical recognition domains.

https://doi.org/10.1038/s41556-022-01005-8

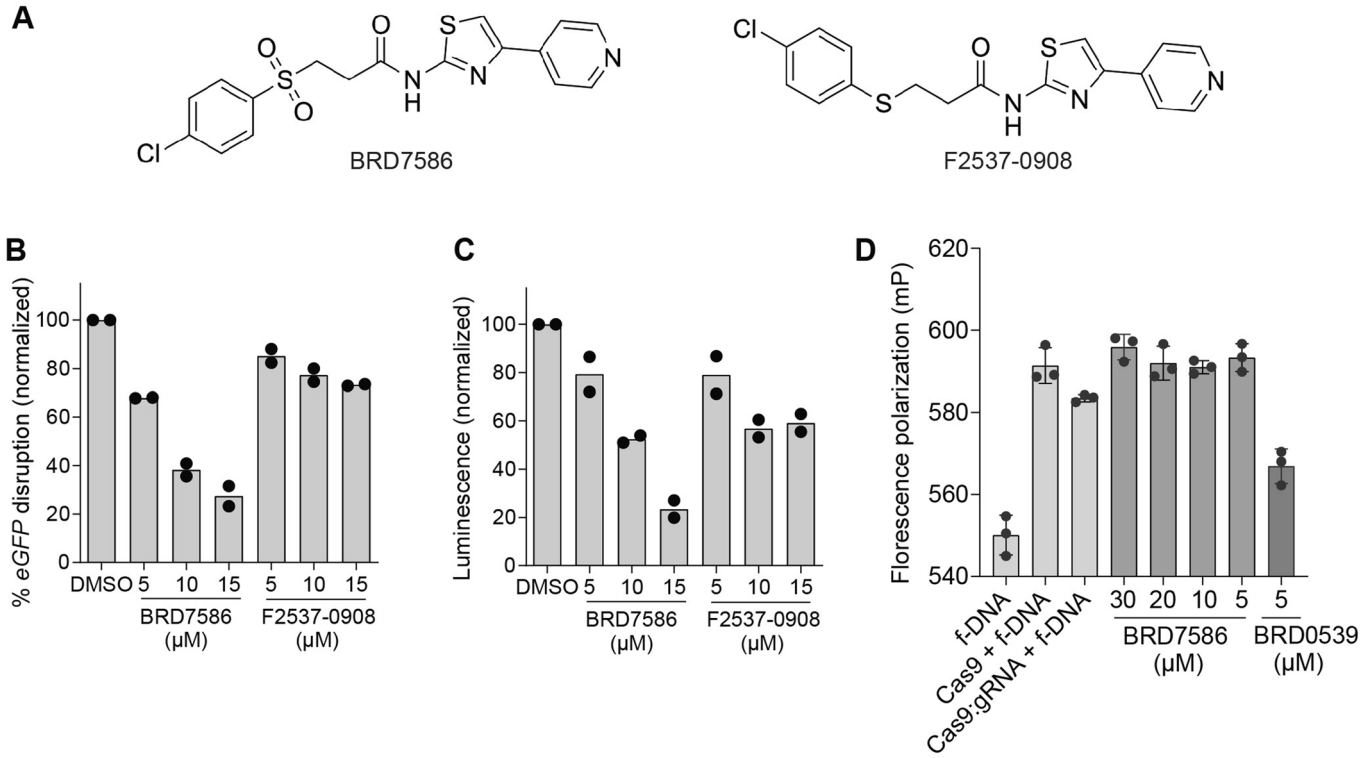

Extended Data Fig. 8 | Mechanism of action studies of BRD7586. (**a**) Structure of BRD7586 and F2537-0908. (**b**) Activity of BRD7586 and F2537-0908 in the eGFP disruption assay. Results from 2 independent experiments are shown. (**c**) Activity of BRD7586 and F2537-0908 in the *HiBiT* knock-in assay. Results from 2 independent replicates are shown. (**d**) Fluorescence polarization assay to detect Cas9–DNA interactions. f-DNA indicates FITC-labelled, SpCas9 PAM-containing DNA. Error bars represent mean ± SD from 3 independent replicates. For BRD0539 at 5 μM compared to DMSO, p = 0.0026 (unpaired t-test, two-tailed).

nature research

Corresponding author(s): Amit Choudhary

Last updated by author(s): Aug 22, 2022

Reporting Summary

Nature Research wishes to improve the reproducibility of the work that we publish. This form provides structure for consistency and transparency in reporting. For further information on Nature Research policies, see our Editorial Policies and the Editorial Policy Checklist.

Statistics

For all statistical analyses, confirm that the following items are present in the figure legend, table legend, main text, or Methods section.

n/a	Confirmed	
☐	☒	The exact sample size (*n*) for each experimental group/condition, given as a discrete number and unit of measurement
☐	☒	A statement on whether measurements were taken from distinct samples or whether the same sample was measured repeatedly
☐	☒	The statistical test(s) used AND whether they are one- or two-sided *Only common tests should be described solely by name; describe more complex techniques in the Methods section.*
☒	☐	A description of all covariates tested
☐	☒	A description of any assumptions or corrections, such as tests of normality and adjustment for multiple comparisons
☐	☒	A full description of the statistical parameters including central tendency (e.g. means) or other basic estimates (e.g. regression coefficient) AND variation (e.g. standard deviation) or associated estimates of uncertainty (e.g. confidence intervals)
☐	☒	For null hypothesis testing, the test statistic (e.g. *F*, *t*, *r*) with confidence intervals, effect sizes, degrees of freedom and *P* value noted *Give P values as exact values whenever suitable.*
☒	☐	For Bayesian analysis, information on the choice of priors and Markov chain Monte Carlo settings
☒	☐	For hierarchical and complex designs, identification of the appropriate level for tests and full reporting of outcomes
☒	☐	Estimates of effect sizes (e.g. Cohen's *d*, Pearson's *r*), indicating how they were calculated

Our web collection on statistics for biologists contains articles on many of the points above.

Software and code

Policy information about availability of computer code

Data collection	PerkinElmer Envision Manager 1.13, Molecular Devices MetaXpress, PerkinElmer Operetta Harmony 4.8, Molecular Devices SoftMax Pro 7.0, Azure Biosystems Azure 600, LI-COR Image Studio, MiSeq Control Software, Topspin 3.5
Data analysis	GraphPad Prism 8, Microsoft Excel 2016, Molecular Devices MetaXpress, PerkinElmer Operetta Harmony 4.8, ImageJ 1.52a, Schrödinger Maestro v12.1, MNova software package, CRISPResso 2, Proteome Discoverer 2.3

For manuscripts utilizing custom algorithms or software that are central to the research but not yet described in published literature, software must be made available to editors and reviewers. We strongly encourage code deposition in a community repository (e.g. GitHub). See the Nature Research guidelines for submitting code & software for further information.

Data

Policy information about availability of data

All manuscripts must include a data availability statement. This statement should provide the following information, where applicable:

- Accession codes, unique identifiers, or web links for publicly available datasets
- A list of figures that have associated raw data
- A description of any restrictions on data availability

Data generated in this study are provided in the manuscript, Supplementary Information, and Source Data. All other data supporting the findings of this study are available from the corresponding author on reasonable request. Plasmids from Addgene (#43861 [https://www.addgene.org/43861], #47511 [https://www.addgene.org/47511], #42230 [https://www.addgene.org/42230]) were used in this study. Structural information from PDB (ID: 5F9R [https://www.rcsb.org/structure/5F9R]) was used in this study. High-throughput sequencing data have been deposited at the NCBI Sequence Read Archive database under accession number PRJNA862731.

Field-specific reporting

Please select the one below that is the best fit for your research. If you are not sure, read the appropriate sections before making your selection.

☒ Life sciences ☐ Behavioural & social sciences ☐ Ecological, evolutionary & environmental sciences

For a reference copy of the document with all sections, see nature.com/documents/nr-reporting-summary-flat.pdf

Life sciences study design

All studies must disclose on these points even when the disclosure is negative.

Sample size	Sample size (number of replicates) were chosen based on previous literatures about genome editing (e.g., Nature 517, 583-588 / Cell 177, 1067-1079).
Data exclusions	No data were excluded from the analyses.
Replication	At least two biological replicates were used for cellular experiments except for the structure-activity relationship studies (Figure 5), where instead two orthogonal assays were performed to ensure high reliability of the results. Each replicate number of each experiment is provided in the figure legends. All attempts at replication were successful.
Randomization	No randomization was applied; cell culture, treatment, sample preparation, and measurement were performed under the identical conditions.
Blinding	No blinding was applied; cell culture, treatment, sample preparation, and measurement were performed under the identical conditions.

Reporting for specific materials, systems and methods

We require information from authors about some types of materials, experimental systems and methods used in many studies. Here, indicate whether each material, system or method listed is relevant to your study. If you are not sure if a list item applies to your research, read the appropriate section before selecting a response.

Materials & experimental systems

n/a	Involved in the study
☐	☒ Antibodies
☐	☒ Eukaryotic cell lines
☒	☐ Palaeontology and archaeology
☒	☐ Animals and other organisms
☒	☐ Human research participants
☒	☐ Clinical data
☒	☐ Dual use research of concern

Methods

n/a	Involved in the study
☒	☐ ChIP-seq
☒	☐ Flow cytometry
☒	☐ MRI-based neuroimaging

Antibodies

Antibodies used	Rabbit anti-SpCas9 (Abcam #189380, 1:1,000 dilution), Mouse anti-SpCas9 (Abcam #191468, 1:1,000 dilution), Mouse anti-α-tubulin (Cell Signaling Technology #3873, 1:2,000 dilution), IRDye 680RD Donkey anti-Rabbit IgG (LI-COR #925-68073, 1:10,000 dilution), IRDye 800CW Donkey anti-Mouse IgG (LI-COR #925-32212, 1:10,000 dilution), anti-Mouse IgG-HRP (Cell Signaling Technology #7076, 1:5,000 dilution).
Validation	Abcam (ab189380): Rabbit monoclonal [EPR18991] to CRISPR-Cas9 validated by the supplier as a primary antibody for western blot using whole cell lysate from HEK-293 transfected with SpCas9. Abcam (ab191468): Mouse monoclonal [7A9-3A3] to CRISPR-Cas9 validated by the supplier as a primary antibody for western blot using whole cell lysate from NIH 3T3 overexpressing SpCas9. Cell Signaling Technology (3873): α-Tubulin (DM1A) Mouse mAb validated by the supplier as a primary antibody in western blot using extracts from HeLa cells. Human α-Tubulin was detected using this antibody. LI-COR (925-68073): IRDye® 680RD Donkey anti-Rabbit IgG Secondary Antibody validated by the supplier as a secondary antibody for western blot. LI-COR (925-32212): IRDye® 800CW Donkey anti-Mouse IgG Secondary Antibody validated by the supplier as a secondary antibody for western blot. Cell Signaling Technology (7076): Anti-mouse IgG, HRP-linked Antibody validated by the supplier as a secondary antibody for western blot.

Eukaryotic cell lines

Policy information about cell lines

Cell line source(s)	U2OS.eGFP.PEST cells were obtained from Keith Joung's lab. HEK293T cells were obtained from ATCC (ATCC #CRL-3216).
Authentication	None of the cell line was authenticated.
Mycoplasma contamination	Cell lines were routinely tested for Mycoplasma contamination using the Universal Mycoplasma Detection Kit (ATCC, #30-1012K). Cell lines were Mycoplasma-negative.
Commonly misidentified lines (See ICLAC register)	None of the misidentified cell line was used.